

Observational constraints on Arctic Ocean clouds and radiative fluxes during the early 21st century

Jennifer E. Kay¹ and Tristan L'Ecuyer²

Received 18 March 2013; revised 9 May 2013; accepted 12 May 2013; published 8 July 2013.

[1] Arctic Ocean observations are combined to create a cloud and radiation climatology for the early 21st century (March 2000 to February 2011). Data sources include: active (CloudSat, CALIPSO) and passive (MODIS) satellite cloud observations, observed top-of-atmosphere (TOA) radiative fluxes (CERES-EBAF), observationally constrained radiative flux calculations (2B-FLXHR-LIDAR), and observationally constrained cloud forcing calculations (CERES-EBAF, 2B-FLXHR-LIDAR). Uncertainty in flux calculations is dominated by cloud uncertainty, not surface albedo uncertainty. The climatology exposes large geographic, seasonal, and interannual variability cloud forcing, but on average, Arctic Ocean clouds warm the surface ($+10 \text{ W m}^{-2}$, in 2B-FLXHR-LIDAR) and cool the TOA (-12 W m^{-2} , in CERES-EBAF and 2B-FLXHR-LIDAR). Shortwave TOA cloud cooling and longwave TOA cloud warming are stronger in 2B-FLXHR-LIDAR than in CERES-EBAF, but these two differences compensate each other, yielding similar net TOA values. During the early 21st century, summer TOA albedo decreases are consistent with sea ice loss but are unrelated to summer cloud trends that are statistically insignificant. In contrast, both sea ice variability and cloud variability contribute to interannual variability in summer shortwave radiative fluxes. Summer 2007 had the largest persistent cloud, radiation, and sea ice anomalies in the climatology. During that summer, positive net shortwave radiation anomalies exceeded 20 W m^{-2} over much of the Arctic Ocean. This enhanced shortwave absorption resulted primarily from cloud reductions during early summer and sea ice loss during late summer. In summary, the observations show that while cloud variability influences absorbed shortwave radiation variability, there is no summer cloud trend affecting summer absorbed shortwave radiation.

Citation: Kay, J. E., and T. L'Ecuyer (2013), Observational constraints on Arctic Ocean clouds and radiative fluxes during the early 21st century, *J. Geophys. Res. Atmos.*, 118, 7219–7236, doi:10.1002/jgrd.50489.

1. Motivation and Paper Goals

[2] Arctic sea ice loss and greater-than-global-average Arctic surface warming have accelerated during the early 21st century. While both internal variability and anthropogenic forcing contribute to observed Arctic climate change and variability [e.g., *Serreze et al.*, 2007; *Kay et al.*, 2011], the underlying processes remain poorly observed. Since 2000, new satellite observations of Arctic cloud distributions and radiative fluxes have become available. Motivated by the need to understand Arctic variability and change and the availability of a large number of complementary observations, the goal of this study is to combine satellite data sets to

document observational constraints on Arctic Ocean clouds and radiative fluxes during the early 21st century. We create an Arctic Ocean climatology with data sets available over the 11 year period from March 2000 to February 2011 (Table 1). We then use the climatology both to evaluate the influence of clouds on Arctic Ocean radiative fluxes and to assess relationships between Arctic Ocean clouds, radiative fluxes, and sea ice.

2. Data Sets

[3] Observations from Clouds and the Earth's Radiant Energy System–Energy Balanced and Filled (CERES-EBAF) [*Loeb et al.*, 2009] provide the only available constraint on Arctic Ocean radiative fluxes. As described in *Loeb et al.* [2009], CERES-EBAF fluxes are adjusted within their uncertainty range to remove the inconsistency between the global average net top-of-atmosphere (TOA) flux and heat storage in the earth-atmosphere system. Observational errors in CERES-EBAF shortwave and longwave TOA fluxes are estimated to be less than 5 W m^{-2} (N. Loeb, personal communication, 2012). CERES-EBAF radiative flux observations also provide a trusted benchmark for validating

¹Climate and Global Dynamics, National Center for Atmospheric Research, Boulder, Colorado, USA.

²Department of Atmospheric and Oceanic Sciences, University of Wisconsin, Madison, Wisconsin, USA.

Corresponding author: J. E. Kay, Climate and Global Dynamics, National Center for Atmospheric Research, Boulder, CO 80305, USA. (jenkay@ucar.edu)

©2013. American Geophysical Union. All Rights Reserved.
2169-897X/13/10.1002/jgrd.50489

Table 1. Arctic Ocean Cloud and Radiation Data Sets for the Early 21st Century Climatology^a

Name	Variable	Time Period	Version	Reference
CERES-EBAF	top-of-atmosphere (TOA) radiative fluxes and TOA cloud forcing	11 years, March 2000 to February 2011	version 2.6	<i>Loeb et al. [2009]</i>
MODIS	total cloud fraction	11 years, June, July, and August 2000–2010 only	Cloud_Fraction_Day_Mean (CF), Level-3, collection 5.1 product ^b	<i>Platnick et al. [2003]</i> and <i>Liu et al. [2010]</i>
2B-FLXHR-LIDAR	TOA and surface radiative fluxes and cloud forcing	almost 5 years, July 2006 to February 2011	RO4.P2-ERB	<i>Henderson et al. [2013]</i> and this study for polar regions
Colocated CloudSat + CALIPSO	total cloud fraction	almost 5 years, July 2006 to February 2011	R04 2B-GEOPROF and R04.P2 2B-GEOPROF-LIDAR combined as in <i>Kay and Gettelman [2009]</i>	<i>Mace et al. [2009]</i> and <i>Marchand et al. [2008]</i>

^aThe Arctic Ocean domain is herein defined as open water or sea ice covered areas poleward of 70°N. The start date for the climatology (March 2000) coincides with the availability of MODIS and CERES-EBAF observations. The end date for the climatology (February 2011) coincides with the loss of combined colocated CloudSat + CALIPSO observations.

^b*Liu et al. [2010]* found Cloud_Fraction_Combined_Fmean (CFC) is more affected by the ocean surface properties than CF. They advise against using CFC in cloud amount studies in the Arctic. We found quantitative differences between CFC and CF, but our results were qualitatively unchanged by using CFC or CF.

observationally constrained radiative transfer calculations. Despite their utility, CERES-EBAF observations have not been used in any of the recent studies that analyze the influence of shortwave radiation anomalies on Arctic sea ice loss [e.g., *Kay et al., 2008*; *Schweiger et al., 2008*; *Graversen et al., 2010*; *Nussbaumer and Pinker, 2012*].

[4] While reanalysis data sets do provide observationally constrained radiative fluxes, the clouds in reanalysis data sets are produced by model parameterizations. Because we elected to not analyze the influence of model-generated clouds on radiative fluxes, reanalysis data sets are not included in this paper. Instead, cloud observations are used to constrain cloud amounts and radiative transfer calculations of Arctic Ocean radiative fluxes and cloud forcing. Fortunately, unique complementary spaceborne cloud observations are available during the early 21st century including the colocated radar CloudSat and lidar CALIPSO [*Stephens et al., 2008*; *L'Ecuyer and Jiang, 2010*] and the passive multispectral Moderate Resolution Imaging Spectroradiometer (MODIS) sensor [*Platnick et al., 2003*].

[5] CloudSat + CALIPSO are of high value to any cloud study because of their active cloud detection technique and their ability to provide vertical cloud distributions, but they have limited spatiotemporal sampling, are only regularly available and colocated from June 2006 to February 2011, and can miss near-surface clouds due to attenuation and ground clutter. Previous work has shown that CloudSat + CALIPSO provide a unique new constraint on vertical cloud structure and radiative fluxes [e.g., *L'Ecuyer et al., 2008*; *Kay et al., 2008*; *Henderson et al., 2013*].

[6] CloudSat + CALIPSO are especially valuable in the Arctic because they do not rely on contrast with the surface for cloud detection. To date, surface-blind CloudSat + CALIPSO cloud observations have been extensively analyzed in the Arctic [e.g., *Kay and Gettelman, 2009*; *Palm et al., 2010*; *Wu and Lee, 2012*; *Barton et al., 2012*; *Cesana et al., 2012*], but their full potential remains unrealized. For example, combining CloudSat + CALIPSO with other key observational Arctic data sets to constrain radiative transfer calculations has great potential to advance constraints on Arctic cloud forcing.

[7] Unlike CloudSat + CALIPSO, MODIS cloud detection uses passive techniques that rely on contrast with the surface and an underlying surface mask. *Liu et al. [2010]* show that MODIS cloud detection retrievals perform better over the ocean than over ice and, as a consequence, MODIS data have unrealistically large increases in cloud amount from ice-covered to open water ocean surfaces. When CloudSat + CALIPSO have sufficient sampling, their detected cloud anomalies are more reliable than those from MODIS. In spite of these known problems, MODIS cloud retrievals over the Arctic Ocean are used in this analysis. The sampling and coincident availability with CERES-EBAF make MODIS cloud observations invaluable for assessing cloud trends and variability. Whenever possible, CloudSat + CALIPSO cloud anomalies are compared to MODIS cloud anomalies in this work.

[8] Effectively combining polar data sets to constrain radiative fluxes is an ambitious endeavor that previous studies have left incomplete (e.g., no incorporation of CALIPSO-detected clouds [*Zygmuntowska et al., 2012*] and no incorporation of interannual variations in surface

Table 2. Ice-/Snow-Covered Surface Albedos for Each Shortwave Spectral Band Specified in the 2B-FLXHR-LIDAR Algorithm^a

	Wavelength					
	0.659 μm	0.858 μm	1.24 μm	1.64 μm	2.13 μm	3.74 μm
Dry season albedo	0.9	0.85	0.45	0.15	0.15	0.05
Melt season albedo	0.85	0.75	0.25	0.05	0.05	0.05

^aAlbedos are based on *Briegleb and Ramanathan [1982]* and *Bowker et al. [1985]*. The Arctic melt season is defined as 1 June through 31 August.

Table 3. Arctic Ocean Top-of-Atmosphere (TOA) Fluxes From CERES-EBAF Observations and 2B-FLXHR-LIDAR Calculations^a

	Incoming Shortwave Radiation	Outgoing Shortwave Radiation	Outgoing Longwave Radiation	Net TOA Radiation
CERES-EBAF (70–90°N; March 2000 to February 2011)	183	98	201	–116
CERES-EBAF (70–90°N; July 2006 to February 2011)	183	96	202	–115
CERES-EBAF (70–82°N; July 2006 to February 2011)	185	95	203	–113
2B-FLXHR-LIDAR (70–82°N; July 2006 to February 2011)	186	86	197	–97

^aAll values in W m^{-2} .

albedo [Kay *et al.*, 2008]). This study aims to improve on these previous observationally constrained radiative transfer calculations using a level 2 CloudSat data product called 2B-FLXHR-LIDAR (Table 1 and Henderson *et al.* [2013]). As such, algorithmic aspects of 2B-FLXHR-LIDAR are next described. The 2B-FLXHR-LIDAR contains radiative fluxes and atmospheric heating rates constrained by observations from the A-train satellite constellation and by atmospheric temperature and humidity, and sea surface temperatures from time-coincident European Centre for Medium-Range Weather Forecasts analyses. While an earlier version used only CloudSat to constrain clouds (2B-FLXHR [L'Ecuyer *et al.*, 2008]), 2B-FLXHR-LIDAR combines CloudSat, CALIPSO, and MODIS observations to constrain the influence of clouds on radiative fluxes. Incorporating the radiative influence of optically thin and low clouds that went undetected by CloudSat significantly improved agreement between 2B-FLXHR-LIDAR calculations and CERES observations. Henderson *et al.* [2013] provide a description of the base algorithm used in 2B-FLXHR-LIDAR and characterize global 2B-FLXHR-LIDAR uncertainties using a combination of sensitivity studies and comparisons with TOA CERES observations. Globally, 2B-FLXHR-LIDAR outgoing shortwave radiation (OSR) agrees to within 4 W m^{-2} of collocated TOA CERES observations with root-mean-square differences of 16 W m^{-2} on monthly/ 5° scales. Global mean OSR and outgoing longwave radiation (OLR) estimated from collocated CERES observations and 2B-FLXHR-LIDAR calculations agree to within 4 and 5 W m^{-2} , respectively, with root-mean-square differences of 6 W m^{-2} and 16 W m^{-2} on monthly/ 5° scales.

[9] In this study, two improvements are made to the 2B-FLXHR-LIDAR algorithm described in Henderson *et al.* [2013] that are important for Arctic radiative flux calculations. First, even though the full diurnal cycle of cloud cover is not measured by the A-train, we have accounted for diurnal variations in solar incidence angle and incoming solar radiation. Specifically, 2B-FLXHR-LIDAR radiative transfer calculations are done every 2 h with the closest available A-train observations and with time-varying solar zenith angle and insolation values.

[10] Second, we have implemented a more sophisticated treatment of surface albedo for polar regions within the 2B-FLXHR-LIDAR framework. Specifically, the time-varying surface albedo is specified based on the National Snow and Ice Data Center Near-real-time Ice and Snow Extent (NISE1) product [Nolin *et al.*, 1998]. The NISE1 data set provides daily estimates of sea ice concentration and snow extent at 25 km resolution from passive microwave instruments aboard the Defense Meteorological Satellite Program satellites. The wavelength-dependent albedo over snow- and ice-covered surfaces is specified according to Table 2. Though this incorporation

of daily varying snow and ice distributions leads to a more accurate representation of surface albedo in 2B-FLXHR-LIDAR, the treatment of surface albedo in 2B-FLXHR-LIDAR is still highly idealized and could be improved. For example, the surface albedo could be parameterized to represent changes related to processes such as snow aging and melt pond formation. These processes have been shown to cause sea ice albedos to range from 0.20 to 0.85 locally [e.g., Perovich and Polashenski, 2012] and would reduce the surface albedos in 2B-FLXHR-LIDAR, especially late in the melt season. That said, constraining local variations in sea ice albedo at the scales examined here is challenging, and we opted for simplicity in this study.

[11] Compared to CERES-EBAF observations, 2B-FLXHR-LIDAR calculations are available for a shorter time period (July 2006 to February 2011) and have an observational “pole hole” from 82 to 90°N. Because CERES-EBAF

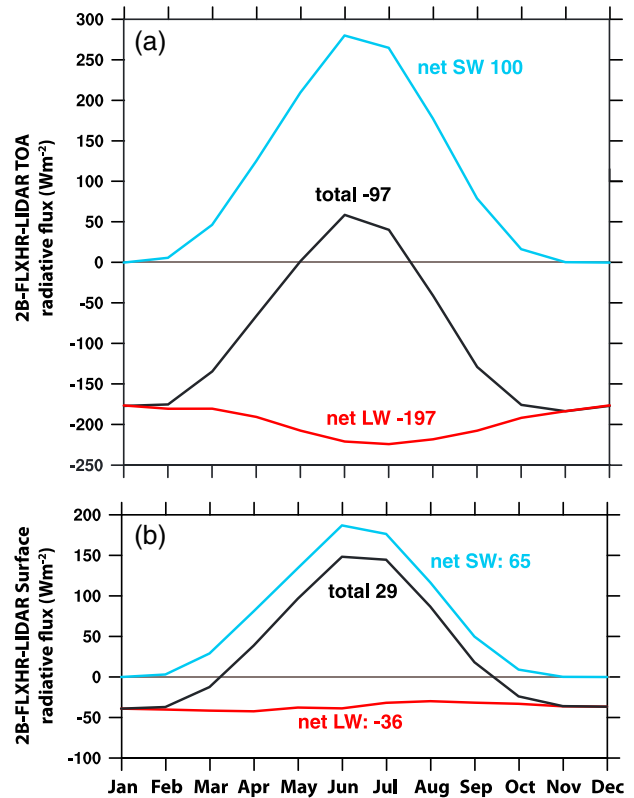


Figure 1. Monthly mean Arctic Ocean (70–82°N) radiative fluxes from 2B-FLXHR-LIDAR: (a) TOA and (b) surface. Annual mean values are reported in the figure panels. The figure uses 2B-FLXHR-LIDAR data available from July 2006 to February 2011 (Table 1).

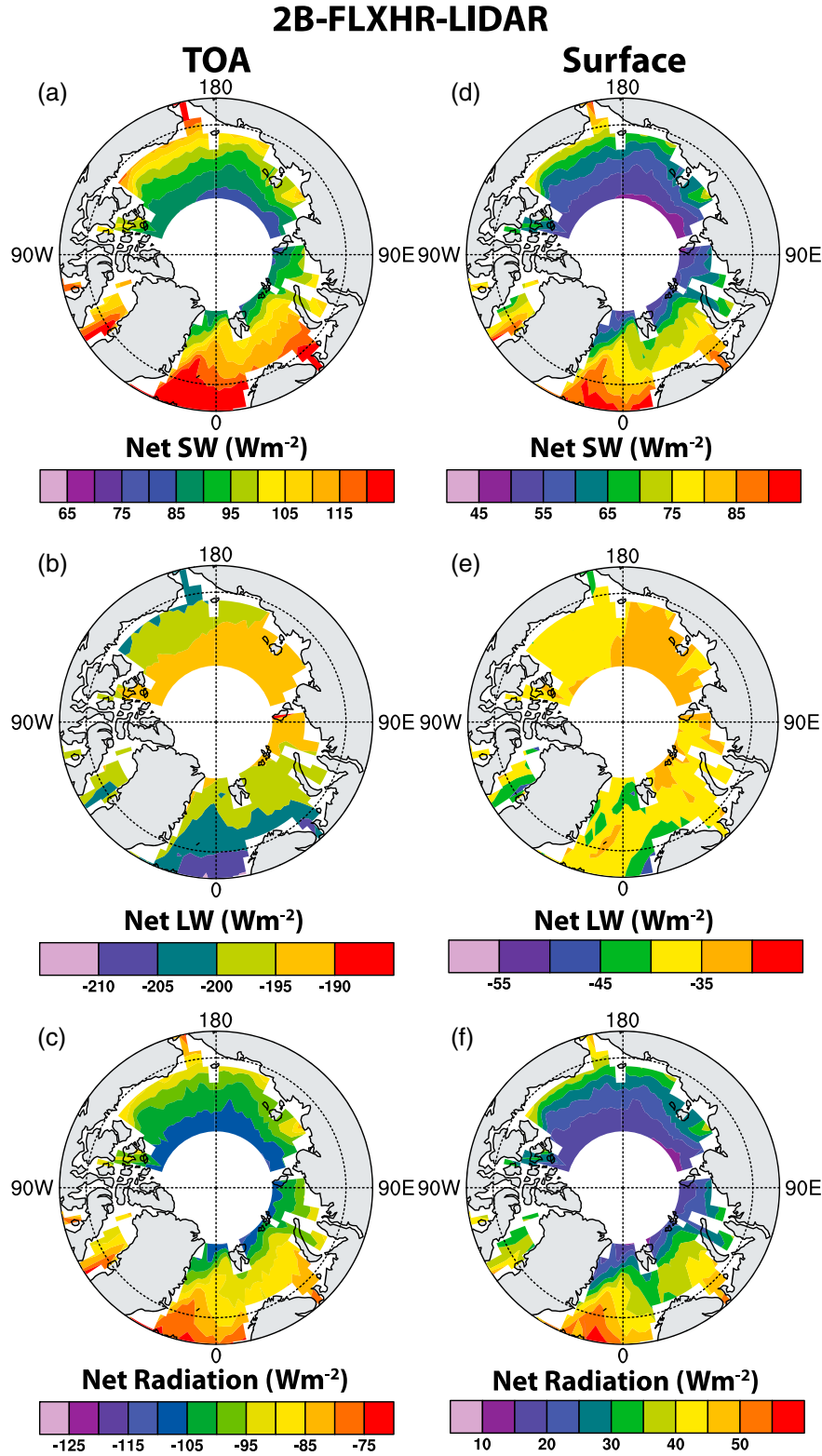


Figure 2. Polar maps of annual mean Arctic Ocean radiative fluxes from 2B-FLXHR-LIDAR: (a) TOA net shortwave radiation, (b) TOA net longwave radiation, (c) TOA net radiation, and (d–f) as in Figures 2a–2c but for the surface. The figure uses 2B-FLXHR-LIDAR data available from July 2006 to February 2011 (Table 1).

observations are available over a longer time period (March 2000 to February 2011) and at all latitudes, they can be used to quantify and assess the importance of the shorter data record and pole hole in 2B-FLXHR-LIDAR (Table 3). The

comparisons in Table 3 suggest that temporal sampling and the pole hole introduce $< 3 \text{ W m}^{-2}$ uncertainties to annual mean flux comparisons between 2B-FLXHR-LIDAR and CERES-EBAF. Errors of this magnitude are within the

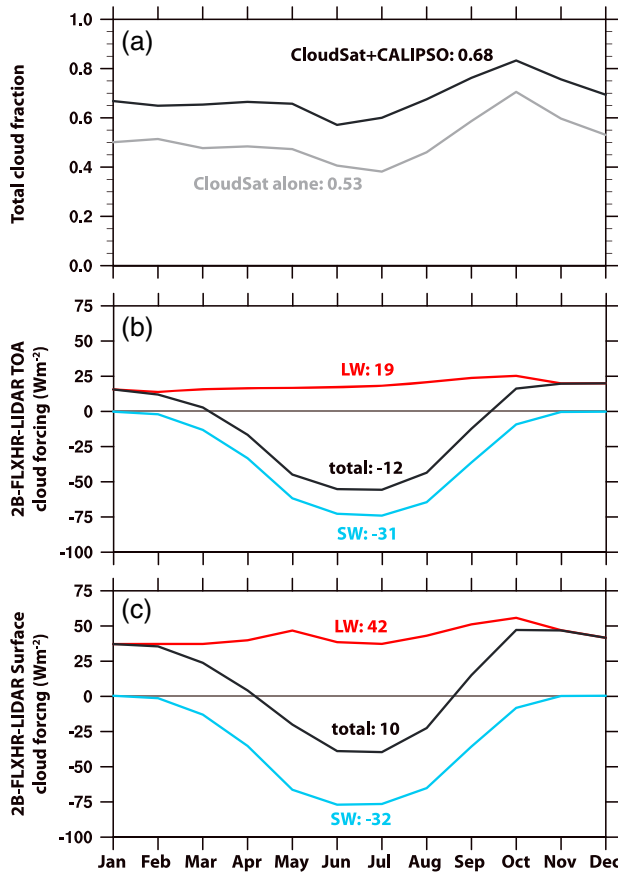


Figure 3. Monthly mean Arctic Ocean (70–82°N) cloud fractions from CloudSat + CALIPSO and cloud forcing from 2B-FLXHR-LIDAR: (a) total cloud fraction from CloudSat + CALIPSO and CloudSat alone, (b) TOA cloud forcing, and (c) surface cloud forcing. In Figure 3a, annual mean cloud fractions are reported for CloudSat + CALIPSO and CloudSat alone. In Figures 3b and 3c, annual mean values are reported for 2B-FLXHR-LIDAR. The figure uses CloudSat, CALIPSO, and 2B-FLXHR-LIDAR data available from July 2006 to February 2011 (Table 1).

observational uncertainty of CERES-EBAF and are smaller than the annual mean differences between 2B-FLXHR-LIDAR and CERES-EBAF (Table 3). Yet, because the effects of sampling are not negligible when considering the differences between 2B-FLXHR-LIDAR and CERES-EBAF, CERES-EBAF observations are reported over the same area (70–82°N) and time period (July 2006 to February 2011) when they are used for evaluating 2B-FLXHR-LIDAR.

3. Results

3.1. Early 21st Century Climatology

3.1.1. Average Arctic Ocean Radiative Fluxes From 2B-FLXHR-LIDAR

[12] The mean annual cycle and geographic distribution of Arctic radiative fluxes are presented in Figures 1 and 2, respectively. As expected, incoming solar radiation is a primary driver of monthly and geographic variability in climatological Arctic Ocean radiative fluxes. Monthly mean

net TOA radiation is positive only in June and July when net shortwave radiation gains exceed net longwave radiation losses (Figure 1a). As latitude increases, net TOA radiation becomes more negative because net shortwave radiation decreases faster than net longwave radiation increases (Figures 2a–2c).

[13] In all sunlit months, net shortwave radiation is larger at the TOA than at the surface, a difference that results from shortwave absorption by the atmosphere (Figure 1). Net longwave radiation is positive at the surface and negative at the TOA, a difference that results from longwave absorption and reemission by the atmosphere (the greenhouse effect). Due to the greenhouse effect and absorbed shortwave radiation, Arctic Ocean net surface radiation is positive from April to September and is also positive in its annual mean ($+29 \text{ W m}^{-2}$ total, $+65 \text{ W m}^{-2}$ shortwave, and -36 W m^{-2} longwave) (Figure 1b). Geographic variations in surface net longwave radiation track variations in near-surface air temperature, water vapor, and liquid cloud cover and exhibit much less geographic variability than net surface shortwave radiation (Figures 2d and 2e). As a result, geographic variations in total net surface radiation are largely dictated by net surface shortwave radiation (Figure 2f).

3.1.2. Average Arctic Ocean Cloud Amount and Cloud Forcing From 2B-FLXHR-LIDAR

[14] We next evaluate temporal and geographic variations in Arctic Ocean cloud amount and cloud influence on radiative fluxes. As is standard, cloud influence on radiative fluxes is measured using cloud forcing, the difference between all-sky and clear-sky fluxes [Ramanathan *et al.*, 1989]. The term “cloud forcing” can be used interchangeably with cloud radiative effect and with cloud radiative forcing. In reality, direct observations of cloud forcing are not available because all estimates of cloud forcing rely on a separate clear-sky radiative transfer calculation (as is the case for 2B-FLXHR-LIDAR) or a comparison of temporally averaged fluxes in cloudy and clear-sky conditions (as is the case for CERES-EBAF).

[15] Figure 3 contains the climatological annual cycle of total cloud fraction and cloud forcing over the Arctic Ocean. According to CloudSat + CALIPSO observations (Figure 3a), monthly mean Arctic Ocean cloud fractions are within 0.15 of the annual mean value (0.68). October is the cloudiest month (total cloud fraction = 0.83), while June is the clearest month (total cloud fraction = 0.57). When just CloudSat is used to detect Arctic Ocean clouds, only 78% of the CloudSat + CALIPSO clouds are detected. That almost a quarter of Arctic Ocean CloudSat + CALIPSO clouds are detected by CALIPSO alone provides strong motivation not to rely on just CloudSat-detected clouds to constrain radiative transfer calculations, as was done in Zygmuntowska *et al.* [2012]. Monthly variations in Arctic Ocean cloud fractions from CloudSat + CALIPSO are more constant through the annual cycle than cloud fractions derived from surface observations [Eastman and Warren, 2010, Figure 5; Beesley and Moritz, 1999, Figure 1] or MODIS [Kato *et al.*, 2006, Figure 2; Liu *et al.*, 2010].

[16] We next evaluate cloud forcing averaged over the Arctic Ocean. Annual mean TOA cloud forcing is negative in 2B-FLXHR-LIDAR (-12 W m^{-2} total, -31 W m^{-2} shortwave, and 19 W m^{-2} longwave), indicating that clouds have a cooling effect at the TOA. In contrast, annual mean

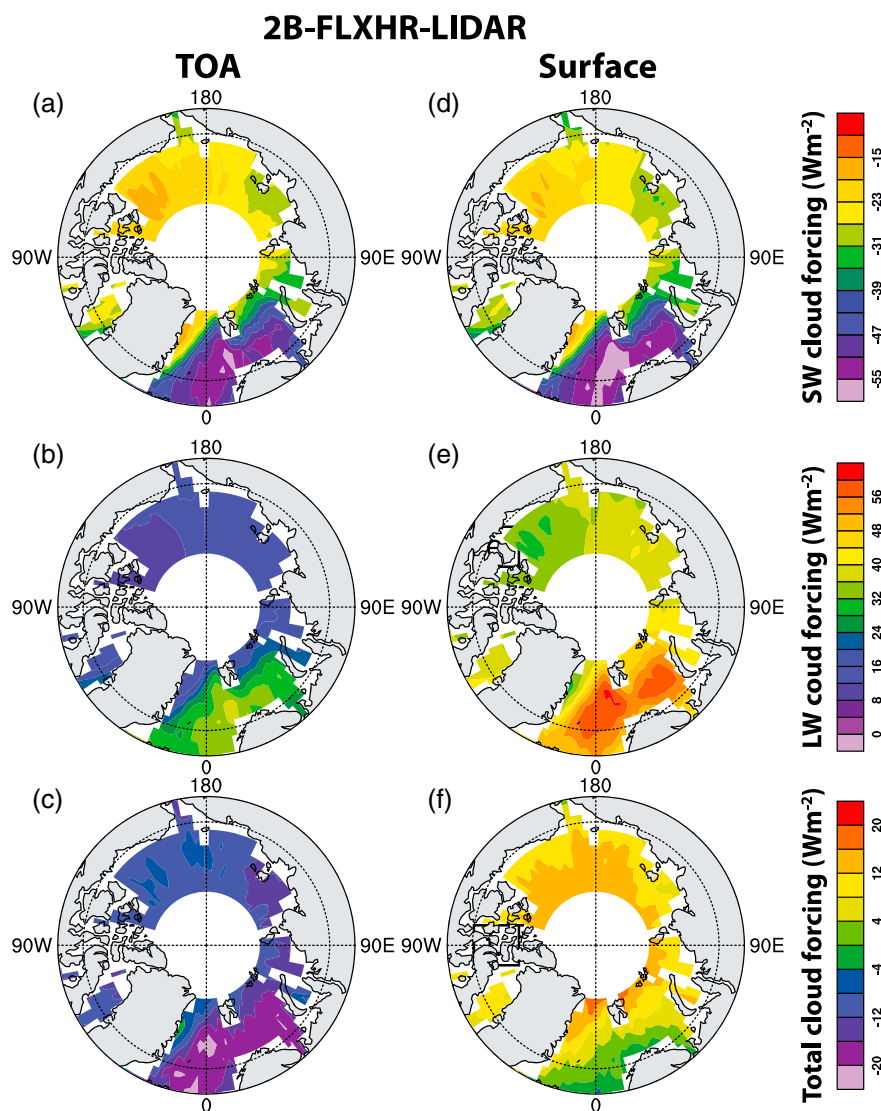


Figure 4. Polar maps of annual mean Arctic Ocean cloud forcing: (a) TOA shortwave cloud forcing, (b) TOA longwave cloud forcing, (c) TOA total cloud forcing, and (d–f) as in Figures 4a–4c but for surface cloud forcing. The figure uses 2B-FLXHR-LIDAR data available from July 2006 to February 2011.

surface cloud forcing is positive in 2B-FLXHR-LIDAR (10 W m^{-2} total, -32 W m^{-2} shortwave, and 42 W m^{-2} longwave), indicating that clouds have a warming effect at the surface.

[17] Comparison of Figure 3a to Figures 3b and 3c reveals that monthly variations in Arctic cloud forcing are more related to incoming solar radiation than to Arctic cloud amount. At the TOA (Figure 3b), Arctic clouds have a warming influence for the dark half of the year (October–March) and a cooling influence for the sunlit half of the year (April–September). At the surface (Figure 3c), the duration of cloud cooling influence is 2 months shorter than that at the TOA (May–August). At both the TOA and the surface, the greatest shortwave cloud cooling occurs during summer months, peaking during June and July.

[18] Figure 4 shows the geographic distributions of climatological annual mean cloud forcing from 2B-FLXHR-LIDAR. Figure 4 shows that shortwave cloud cooling has a similar magnitude and structure at the surface and the TOA but that

longwave cloud warming is approximately twice as strong at the surface as it is at the TOA, as also seen in Figure 3. Because of the competing influences of clouds on net longwave and shortwave radiation, geographic variations in forcing evident for the shortwave and longwave components separately are less evident in total cloud forcing distributions. For example, the decreasing cloud influence on surface radiative fluxes from the Beaufort Sea (150°W) westward to the Laptev Sea (120°E) is less evident in Figure 4f than in Figures 4b and 4d.

[19] While monthly variations in cloud forcing result primarily from monthly variations in solar radiation, Figure 4 suggests that geographic variations in cloud amount exert a strong control on geographic variations in cloud forcing. Previous work has connected Arctic cloud fraction geographic variations to lower tropospheric stability [e.g., Barton *et al.*, 2012; Kay and Gettelman, 2009]. Indeed, Figures 5a and 5b show that annual mean near-surface stability and annual mean total cloud fraction are

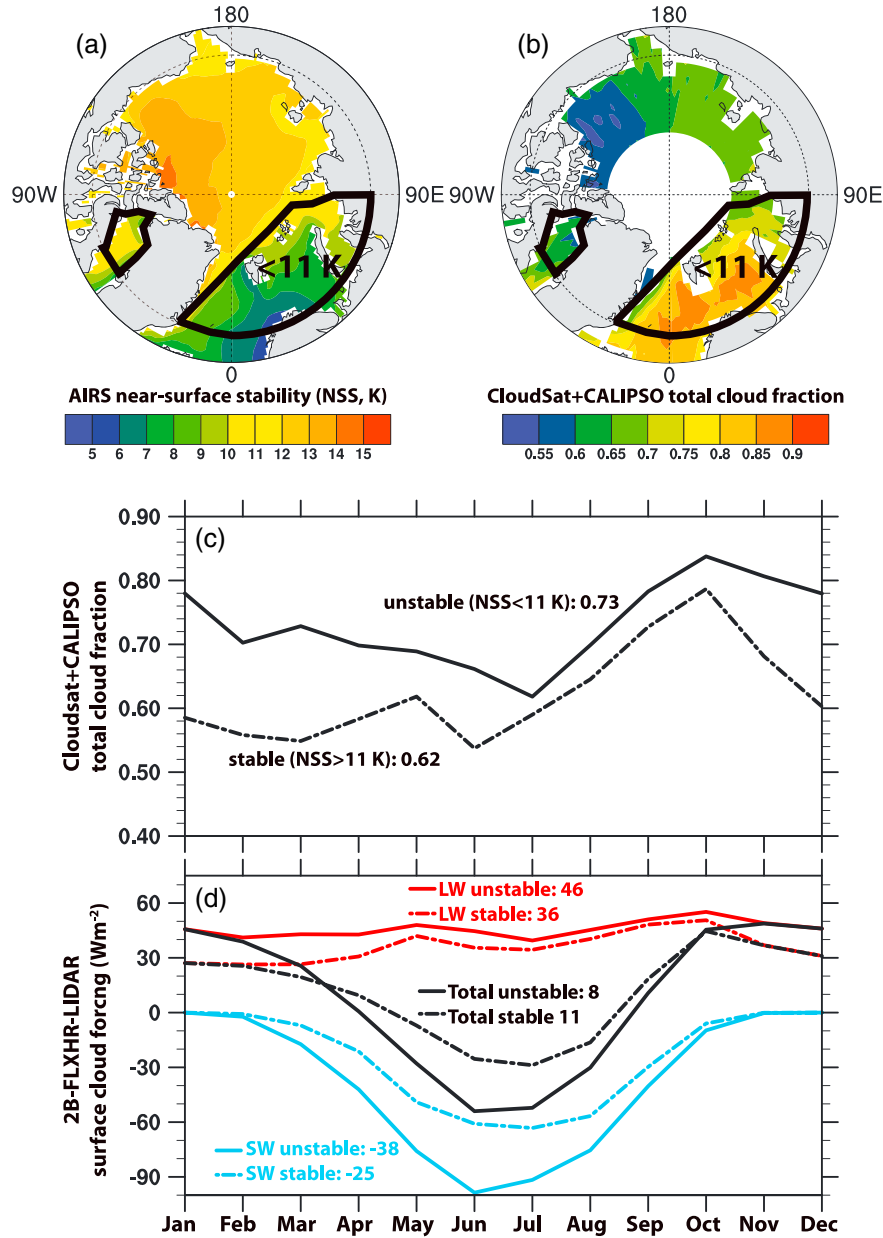


Figure 5. Arctic Ocean (70–82°N) cloud fraction and cloud forcing regimes: (a) polar map of annual mean V4 Atmospheric Infrared Sounder (AIRS) near-surface static stability (NSS, potential temperature at 850 mbar minus potential temperature at 1000 mbar), (b) polar map of annual mean CloudSat + CALIPSO total cloud fraction, (c) monthly evolution of CloudSat + CALIPSO total cloud fraction, and (d) monthly evolution of 2B-FLXHR-LIDAR surface cloud forcing. The figure uses CloudSat + CALIPSO and 2B-FLXHR-LIDAR data available from July 2006 to February 2011 and AIRS data from 2006 to 2009 [Gettelman *et al.*, 2006; Kay and Gettelman, 2009]. The values in Figures 5c and 5d are annual means by regime: unstable (NSS < 11 K) and stable (NSS > 11 K).

spatially anticorrelated: Regions with higher near-surface static stability have fewer clouds. To illustrate the influence of near-surface stability on cloud amount and cloud forcing, we divide the Arctic Ocean into two regimes: stable and unstable. The unstable regime (near-surface stability < 11 K) occurs in the North Atlantic and is associated with the semipermanent Icelandic Low. The high-stability regime (near-surface stability > 11 K) occurs over the central Arctic Ocean. Figures 5c and 5d show the unstable regime has more

cloud and stronger shortwave cloud cooling and longwave cloud warming than the stable regime; however, the total surface cloud forcing is greater in the stable regime than in the unstable regime (11 W m⁻² versus 8 W m⁻²).

3.1.3. Evaluation of Uncertainties in 2B-FLXHR-LIDAR and CERES-EBAF

[20] Observed CERES-EBAF TOA fluxes provide a benchmark for evaluation of the calculated 2B-FLXHR-LIDAR TOA fluxes. Over the same Arctic Ocean region

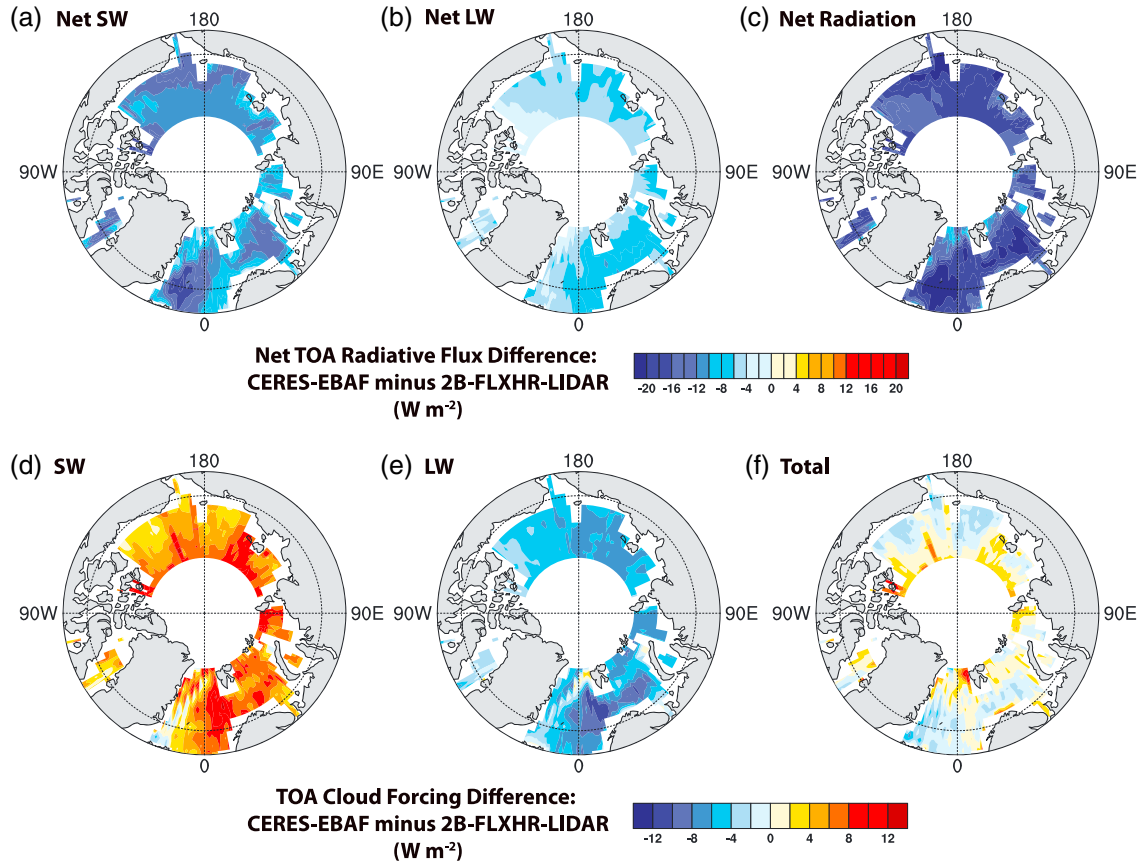


Figure 6. Polar maps of annual mean Arctic Ocean TOA differences (CERES-EBAF minus 2B-FLXHR-LIDAR): (a) net shortwave radiation, (b) net longwave radiation, (c) net radiation, (d) shortwave cloud forcing, (e) longwave cloud forcing, and (f) total cloud forcing. The figure uses 2B-FLXHR and CERES-EBAF data available from July 2006 to February 2011 (Table 1).

(70–82°N) and an overlapping time period (July 2006 to February 2011), the annual mean net TOA flux in 2B-FLXHR-LIDAR calculations (-97 W m^{-2}) is 16 W m^{-2} larger than that in CERES-EBAF observations (-113 W m^{-2}). This difference can be traced to a combination of a 9 W m^{-2} deficit in OSR and a 6 W m^{-2} deficit in OLR in the 2B-FLXHR-LIDAR relative to CERES-EBAF (Table 3). These differences lie within the combined uncertainties of CERES-EBAF ($< 5 \text{ W m}^{-2}$) and 2B-FLXHR-LIDAR (global uncertainties reported in *Henderson et al.* [2013] are $\sim 5 \text{ W m}^{-2}$ for OLR and $\sim 7 \text{ W m}^{-2}$ for OSR). Yet, because these Arctic Ocean TOA flux differences between CERES-EBAF and 2B-FLXHR-LIDAR are appreciable, they merit further investigation.

[21] Figures 6a–6c show that net TOA flux differences between 2B-FLXHR and CERES-EBAF fluxes are evident over the entire Arctic Ocean. At the TOA, the largest monthly mean net shortwave flux differences between 2B-FLXHR-LIDAR calculations and CERES-EBAF observations occur in the late spring and early summer for shortwave radiation (not shown). View angles, field of view, sampling differences, and 2B-FLXHR-LIDAR calculation inputs are candidates to explain these differences. Because the surface albedos assumed in 2B-FLXHR-LIDAR are likely biased high during the late melt

season, surface albedo is not a likely candidate to explain greater absorbed shortwave radiation in 2B-FLXHR-LIDAR calculations as compared to CERES-EBAF observations. Sensitivity tests are needed to understand the differences between 2B-FLXHR-LIDAR calculations and CERES-EBAF observations over the Arctic Ocean.

[22] To identify the specific input parameters that lead to the largest uncertainties in 2B-FLXHR-LIDAR flux calculations, we performed sensitivity tests similar to those described in *Henderson et al.* [2013] but for the Arctic region. As in *Henderson et al.* [2013], the sensitivity tests consisted of repeating 2B-FLXHR-LIDAR radiative transfer calculations with major algorithm inputs perturbed by an amount representative of their accuracy. Over the Arctic Ocean, the results (Table 4) indicate that cloud microphysical properties (water content and particle size) and cloud thickness are the largest contributors to uncertainty in the 2B-FLXHR-LIDAR flux calculations, especially at the surface. In contrast to these cloud property uncertainties, uncertainties introduced by errors in the specification of surface albedo were $5\times$ smaller. The relatively weak sensitivity of radiative fluxes to specification of surface albedo and also the OLR being more sensitive to atmospheric temperature than to surface temperature are both consistent with large cloud fractions over the Arctic Ocean (Figure 3a).

Table 4. Sensitivity of Arctic Ocean 2B-FLXHR-LIDAR Outgoing Top-of-Atmosphere (TOA) and Downwelling Surface Radiative Fluxes to Uncertainties in All Relevant Input Data Sets^a

Parameter	Perturbation	Shortwave		Longwave	
		TOA Out (OSR)	Surface Down	TOA Out (OLR)	Surface Down
Annual mean fluxes	none	86	102	197	248
<i>Clouds Detected by CloudSat</i>					
Precipitation	double/remove	±0.1	±0.1	Negligible Sensitivity (NS)	NS
Cloud Liquid Water Content (LWC)	±50%	±2.4	±3.1	±0.3	±0.3
Liquid cloud effective radius R_e	±25%	±3.2	±1.7	±0.9	±0.2
Cloud Ice Water Content (IWC)	±70%	±1.8	±2.1	±3.0	±0.6
Ice cloud R_e	±25%	±1.0	±0.7	±1.4	±0.2
<i>Clouds Detected by CALIPSO and/or MODIS Only</i>					
CALIPSO-only LWC	±20%	±2.4	±2.5	NS	±2.0
CALIPSO-only IWC	double/half	±0.2	±0.1	±0.5	±0.1
<i>All Clouds</i>					
Cloud thickness (top/base)	±240 m	±2.6	±3.0	±0.2	±2.5
<i>Atmospheric and Surface Properties</i>					
T above 500 mbar	±2 K	NS	NS	NS	NS
T below 500 mbar	±2 K	NS	NS	±5.0	±3.5
Q above 500 mbar	±25%	NS	NS	NS	NS
Q below 500 mbar	±25%	±0.6	±1.2	±1.5	±3.2
Surface temperature	±2 K	NS	NS	±0.9	±3.3
Surface albedo	±10%	±0.4	±0.1	NS	NS

^aValues are derived from the difference between up and down perturbations and are reported in W m^{-2} . Detailed description of methods used to generate these Arctic Ocean values is in *Henderson et al.* [2013], who performed a similar analysis for global values.

[23] The sensitivity tests presented in Table 4 suggest that cloud uncertainties could account for the OSR/OLR deficits of $9 \text{ W m}^{-2}/6 \text{ W m}^{-2}$ in 2B-FLXHR-LIDAR when compared to CERES-EBAF (Figures 6a and 6b). In particular, systematic biases in 2B-FLXHR-LIDAR cloud property inputs (too little water content, too large particle sizes, or too geometrically thin) and lower tropospheric temperature inputs (too cold, longwave only) could plausibly explain low biases in 2B-FLXHR-LIDAR outgoing TOA fluxes. Reducing errors in these inputs could thus improve 2B-FLXHR-LIDAR TOA agreement with CERES-EBAF observations. While these sensitivity tests help us understand the influence of specific parameters on flux uncertainty, it is important to emphasize that the uncertainty values in Table 4 do not exactly represent errors in 2B-FLXHR-LIDAR fluxes shown in this paper (e.g., Figures 1 and 2). Random errors are reduced by averaging, so the actual uncertainties depend strongly on the spatial and temporal scale of the analysis. Without independent validation of 2B-FLXHR-LIDAR inputs, it is difficult to separate the random and systematic components of the 2B-FLXHR-LIDAR flux uncertainties.

[24] We next compare 2B-FLXHR-LIDAR and CERES-EBAF cloud forcing calculations (Figures 6d–6f). Despite identical estimates of the annual mean TOA cloud forcing in 2B-FLXHR-LIDAR and CERES-EBAF (-12 W m^{-2}), 2B-FLXHR-LIDAR calculations indicate both stronger shortwave cloud cooling (-31 W m^{-2} versus -25 W m^{-2}) and stronger longwave cloud warming ($+19 \text{ W m}^{-2}$ versus $+13 \text{ W m}^{-2}$) than CERES-EBAF calculations. Thus, compensating differences are responsible for the same annual mean total cloud forcing in 2B-FLXHR-LIDAR and CERES-EBAF.

[25] The difference maps in Figures 6d–6f provide clues as to the origin of these cloud forcing differences. Cloud forcing is stronger in 2B-FLXHR-LIDAR than in CERES-EBAF over the entire Arctic Ocean. Because surface albedo biases cannot explain many of the cloud forcing differences in Figures 6d–6f, we suspect cloud input differences between CERES-EBAF and

2B-FLXHR-LIDAR calculations must also be important. Evidence to support this suspicion comes from the fact that CERES-EBAF cloud amounts are based on MODIS observations. As discussed when describing Figure 3a, MODIS underestimates Arctic cloud amounts when compared to CloudSat+CALIPSO, especially in winter (compare Figure 3a to *Kato et al.* [2006, Figure 2]). Cloud contamination in CERES-EBAF clear-sky calculations would reduce differences between all-sky and clear-sky fluxes and lead to weaker cloud forcing in CERES-EBAF than in 2B-FLXHR-LIDAR.

3.2. Arctic Ocean Anomalies During the Early 21st Century

3.2.1. Domain-Averaged Arctic Ocean Anomalies

[26] Having presented a climatology of Arctic Ocean radiative fluxes and cloud forcing, we next analyze cloud and radiation anomalies during the early 21st century. Departures from the mean state depicted in Figures 1–5 provide observational insights into the role of surface and atmospheric processes in controlling Arctic climate change and variability.

[27] Figure 7 shows a time series of monthly anomalies in Arctic Ocean TOA radiative fluxes from CERES-EBAF observations. Because no direct comparison with 2B-FLXHR-LIDAR is possible on monthly timescales, the anomalies in Figure 7 are based on the entire CERES-EBAF record analyzed in this study (March 2000 to February 2011). During this period, observed TOA shortwave radiative flux anomalies are larger than observed TOA longwave radiative flux anomalies. The largest positive net radiation anomaly occurred in summer 2007, while the largest negative radiation anomaly occurred in summer 2001.

[28] Because summer shortwave radiation anomalies over the Arctic Ocean are relatively large, we examine them further. We analyze observed TOA albedo (outgoing/incoming) instead of observed TOA net shortwave radiation (incoming-outgoing) to normalize/remove differences caused by large

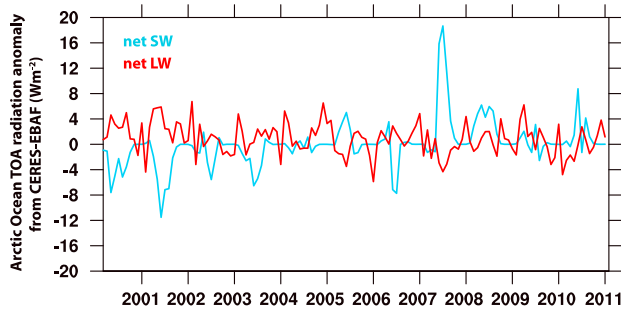


Figure 7. Time series of CERES-EBAF monthly mean TOA Arctic Ocean (70–90°N) radiation anomalies. The figure uses CERES-EBAF data available from March 2000 to February 2011 (Table 1).

monthly variations in solar insolation. We also report anomalies as normalized anomalies (value/mean – 1) to facilitate comparisons between variables. Figure 8a shows a time series of TOA albedo anomalies for each summer month (June, July, and August (JJA)) and for the summer average (JJA). Summer TOA albedos are decreasing from 2000 to 2010, but there is substantial interannual variability about the downward trends. While positive TOA albedo anomalies that occurred during summer 2001 indicate less shortwave radiation was absorbed, large negative TOA albedo anomalies that occurred during summer 2007 indicate more shortwave radiation was absorbed. When measured as an absolute anomaly (value – mean), summer 2007 had 15 W m^{-2} of additional absorbed shortwave radiation and a 3.5% reduction in TOA albedo. It is important to note that these large TOA shortwave anomalies during summer 2007 are from observations, not radiative transfer calculations.

[29] Both the atmosphere and the surface can influence the TOA albedo anomalies time series shown in Figure 8a. Reductions in TOA albedo can result from reduced sea ice or from reduced cloud amounts because summer surface ocean albedos are generally smaller than cloud albedos [Hudson, 2011]. Thus, we next examine time series of cloud fraction anomalies in Figure 8b and sea ice extent anomalies in Figure 8c. Summer cloud fraction anomalies show no visually obvious or statistically significant trend during the early 21st century. In contrast, statistically significant sea ice loss has occurred in all summer months during the early 21st century. In other words, the statistically significant summer TOA albedo decreases over the Arctic Ocean shown in Figure 8a are consistent with statistically significant summer sea ice loss but are not consistent with relatively small and statistically insignificant summer cloud amount changes.

[30] Significant year-to-year variability in both cloud fraction and sea ice extent is evident in the time series shown in Figures 8b and 8c, respectively. Arctic cloud anomalies are most negative during June 2005 and summer 2007 and most positive during June 2006. Arctic sea ice extent anomalies are most negative during August 2007 and most positive during August 2001. While they only overlap for a 5 year period, there is reasonable agreement between independent CloudSat + CALIPSO and MODIS summer cloud anomalies (Figure 8b).

[31] To evaluate relationships between observed variability variations in sea ice extent, cloud, and TOA albedo, we

use the scatterplots and regressions in Figure 9. During JJA, positive statistically significant relationships between TOA albedo anomalies and both cloud anomalies and sea ice extent anomalies are evident. Interestingly, regressions between cloud amount anomalies and ice extent anomalies are not statistically significant (not shown). In other words, sea ice extent variability and cloud amount variability independently contribute to TOA albedo variability over the Arctic Ocean during the early 21st century.

[32] The qualitative agreement between the MODIS and CloudSat + CALIPSO cloud anomalies shown in Figure 8b lends credence to the use of MODIS anomalies at monthly timescales. The regression of monthly MODIS cloud fraction anomalies with monthly TOA albedo anomalies shows that unlike in June and July, the influence of cloud variability

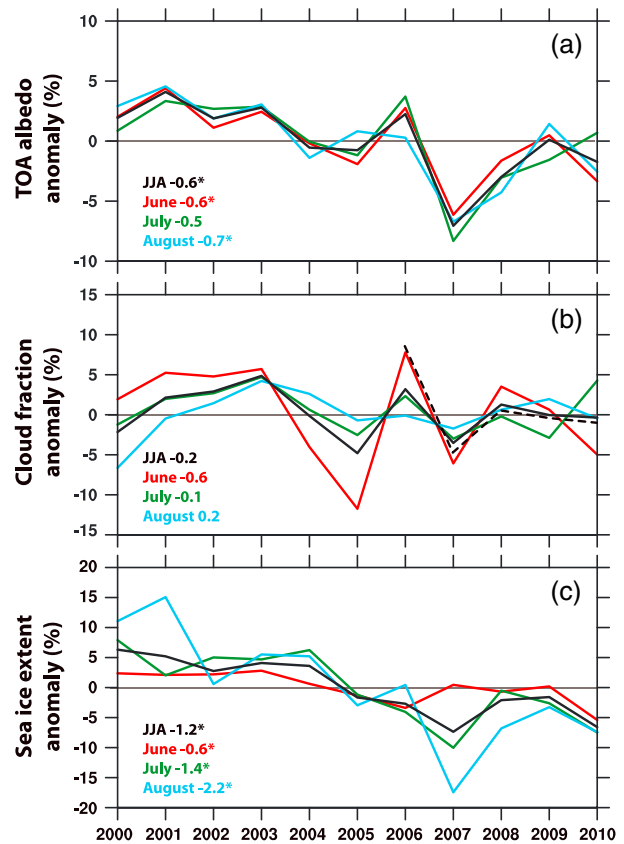


Figure 8. Time series of Arctic Ocean summer (JJA) anomalies: (a) CERES-EBAF TOA albedo, (b) MODIS (solid) and CloudSat + CALIPSO (dashed) total cloud fractions, and (c) Arctic sea ice extent. All anomalies are reported as the percent difference from the mean (value/mean – 1). For each time series, the slope (trend in %/yr) and statistical significance (* if 95% probability of being statistically different than 0 using two-sided Student's *t* test) are provided. MODIS and CERES anomalies were calculated relative to a 2000–2010 mean and for 70–90°N. CloudSat + CALIPSO anomalies were calculated relative to a 2006–2010 mean and for 70–82°N. The figure uses monthly CERES-EBAF, MODIS, and Arctic sea ice data [Fetterer et al., 2002] from March 2000 to February 2011, as well as 2B-FLXHR-LIDAR data available from July 2006 to February 2011 (Table 1).

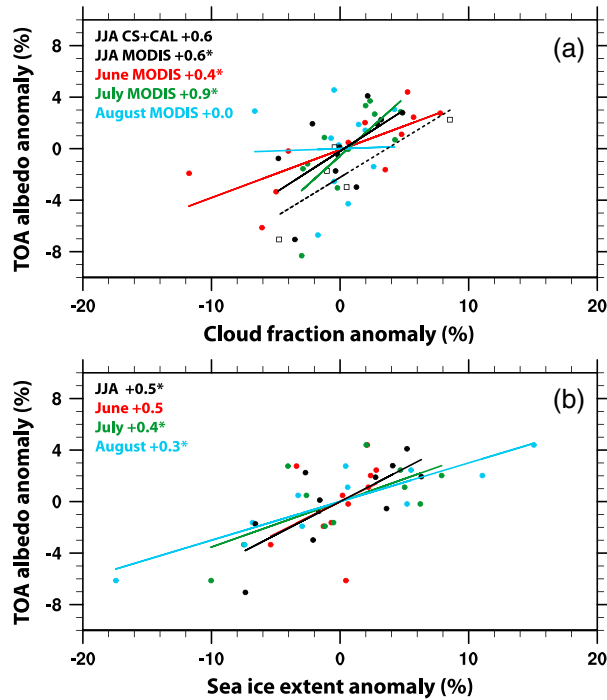


Figure 9. Scatterplots of Arctic Ocean summer (JJA) anomalies: (a) CERES-EBAF TOA albedo versus total cloud fraction from MODIS (filled dots) and CloudSat + CALIPSO (open squares) and (b) CERES-EBAF TOA albedo versus Arctic sea ice extent. For each linear regression, the slope and statistical significance (* if 95% probability of being statistically different than 0 using two-sided Student's t test) are provided. The figure uses the same observations and averaging as Figure 8.

on TOA albedo variability is not statistically significant in August. MODIS-estimated cloud variability is also smaller in August than in June and July. Interestingly, Figure 9b shows that sea ice extent variability is relatively small in June and that relationships between sea ice extent variability and TOA albedo are not statistically significant during this month as they are in July and August. Thus, the regressions in Figure 9 suggest that clouds have a more important influence on TOA albedo anomalies in early summer while sea ice extent anomalies have a more important influence on TOA albedo anomalies in late summer.

3.2.2. Summer 2007 Cloud, Sea Ice, and Shortwave Radiation Anomalies

[33] Because summer 2007 had the largest seasonal Arctic Ocean radiation, cloud, and sea ice anomalies observed within the early 21st century climatology (Figures 7 and 8), we further assess relationships between cloud, radiation, and sea ice anomalies during that summer using observations and an off-line radiative transfer calculation sensitivity test.

[34] First, we examine monthly spatial relationships between shortwave radiation anomalies, cloud anomalies, and the sea ice edge using observations. The anomaly maps in Figure 10 show that both cloud reductions and sea ice loss contributed to positive summer 2007 shortwave radiation anomalies but that their relative importance depended on the month and location. During June 2007, the sea ice edge was at the Arctic Ocean coast (Figure 10a) and sea ice extent

was not anomalous (Figure 8c). Because sea ice covered much of the central Arctic Ocean basin, sea ice anomalies cannot explain the large positive shortwave anomalies evident over much of the Arctic Ocean during June 2007. On the other hand, negative cloud anomalies occurred over almost the entire Arctic Ocean during June 2007 (Figure 10b). Taken together, Figures 10a and 10b provide strong evidence that cloud reductions were the primary contributor to observed shortwave radiation anomalies during June 2007. In July 2007, the sea ice edge moved into the central Arctic Ocean (Figure 10c) and hemispheric sea ice extent was anomalously low (Figure 8c). While the Arctic Ocean areas north of Canada, Alaska, and the Bering Strait all had negative cloud anomalies during July 2007, positive cloud anomalies occur in marginal seas north of Siberia in the East Siberian and Laptev Seas (Figure 10d). Interestingly, Figure 10c shows that the July 2007 sea ice edge corresponds to a step change in the magnitude of the net shortwave radiation anomaly. Where there were open water and reduced cloud cover, the shortwave anomaly exceeded 35 W m^{-2} , while where sea ice cover remained but there was reduced cloud cover, the shortwave anomaly was only $15\text{--}20 \text{ W m}^{-2}$. In August 2007, the sea ice edge retreated further into the Arctic Basin (Figure 10e) and hemispheric sea ice extent was anomalously low (Figure 8c). Cloud anomalies were mostly positive over the Eastern Pacific Arctic but were still negative over the Western Pacific Arctic (Figure 10f). Corresponding to the sea ice and cloud anomalies, the August 2007 net shortwave flux anomalies were smaller in the Eastern Arctic than in the Western Arctic. That said, the largest net TOA shortwave flux anomalies during August 2007 occurred in the Beaufort Sea close to the sea ice edge.

[35] The monthly time resolution of Figure 10 was required to identify the combined influence of cloud anomalies and sea ice loss on seasonal shortwave radiation anomalies. Indeed, it was only by evaluating monthly relationships that the relative contributions of clouds and sea ice loss could be accurately assessed. Looking at seasonal means alone obscures the timing of sea ice loss, cloud anomalies, and shortwave radiations and can therefore be misleading. Unfortunately, the relatively poor sampling of CloudSat + CALIPSO, and therefore 2B-FLXHR-LIDAR, limits analysis of these data sets to seasonal timescales. Despite these sampling limitations, the surface-blind nature of CloudSat + CALIPSO observations provides an invaluable resource for documenting Arctic cloudiness on seasonal and longer timescales and for evaluation of MODIS [e.g., Liu *et al.*, 2010]. As a result, we next evaluate summer cloud spatial pattern anomalies from CloudSat + CALIPSO and compare them to corresponding MODIS anomalies.

[36] Figure 11 shows that large negative summer 2007 total cloud fraction anomalies from CloudSat + CALIPSO and MODIS are colocated with large ($>20 \text{ W m}^{-2}$) positive net TOA shortwave radiation anomalies. While both data sets indicate that summer 2007 had fewer clouds than other summers in the early 21st century, there are differences in their cloud anomaly spatial patterns. For example, comparison of Figure 11a and Figures 11b and 11c shows the negative cloud fraction anomalies in the Chukchi Sea are greater in CloudSat + CALIPSO than in MODIS. In contrast, the negative cloud fraction anomalies in the Beaufort Sea are

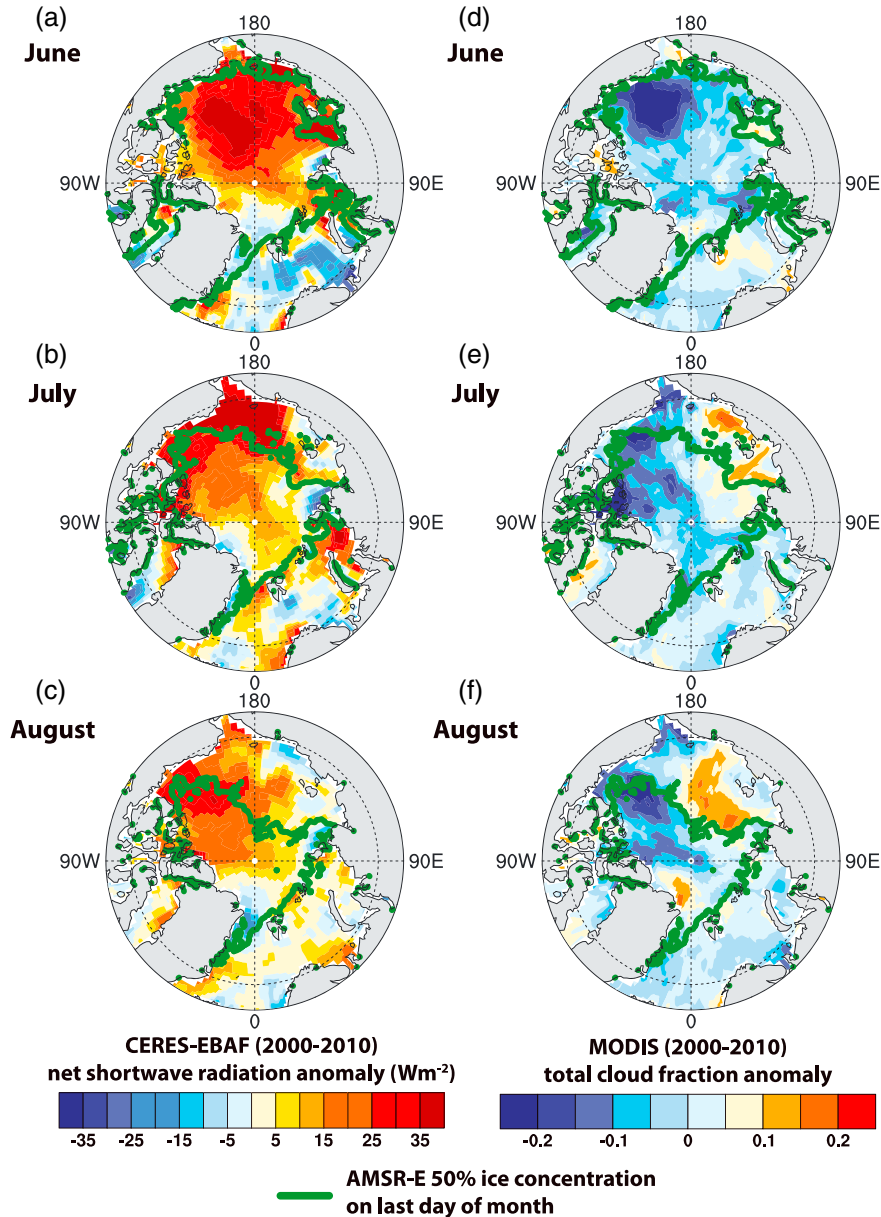


Figure 10. Polar maps of monthly mean anomalies during summer 2007: CERES-EBAF TOA net short-wave radiation anomalies for (a) June 2007, (b) July 2007, and (c) August 2007 and MODIS total cloud fraction anomalies for (d) June 2007, (e) July 2007, and (f) August 2007. The figure uses CERES-EBAF and MODIS data available from March 2000 to February 2011 (Table 1) and daily sea ice extents from Advanced Microwave Scanning Radiometer–EOS (AMSR-E) observations [Cavalieri *et al.*, 2004].

greater in MODIS than in CloudSat+CALIPSO. The qualitative agreement between the MODIS-detected cloud anomalies using different base periods (e.g., 2006–2010 in Figure 11b versus 2000–2010 in Figure 11c) suggests that the base period used for calculating the cloud anomaly has a relatively minor influence on cloud anomaly pattern comparisons.

[37] Given the previously described results of Liu *et al.* [2010], it is not surprising that Figure 11 shows that the MODIS cloud anomalies are more tightly connected to the sea ice edge than CloudSat+CALIPSO cloud anomalies. A tight connection between cloud anomalies and sea ice

anomalies is also seen in Figure 10f. It is however puzzling that the MODIS cloud anomalies shown here are negative in the Chukchi and East Siberian Seas, while they were positive in Schweiger *et al.* [2008, Figure 1c], which used MODIS collection 5. Differences between the Schweiger *et al.* [2008] MODIS cloud anomalies and Figures 10b and 10c cannot be explained by the base period used for anomaly calculations (not shown).

[38] Having presented summer 2007 cloud anomalies, we next evaluate summer 2007 radiative flux anomalies using 2B-FLXHR-LIDAR. The 2B-FLXHR-LIDAR calculations are of particular interest at the surface, where observations

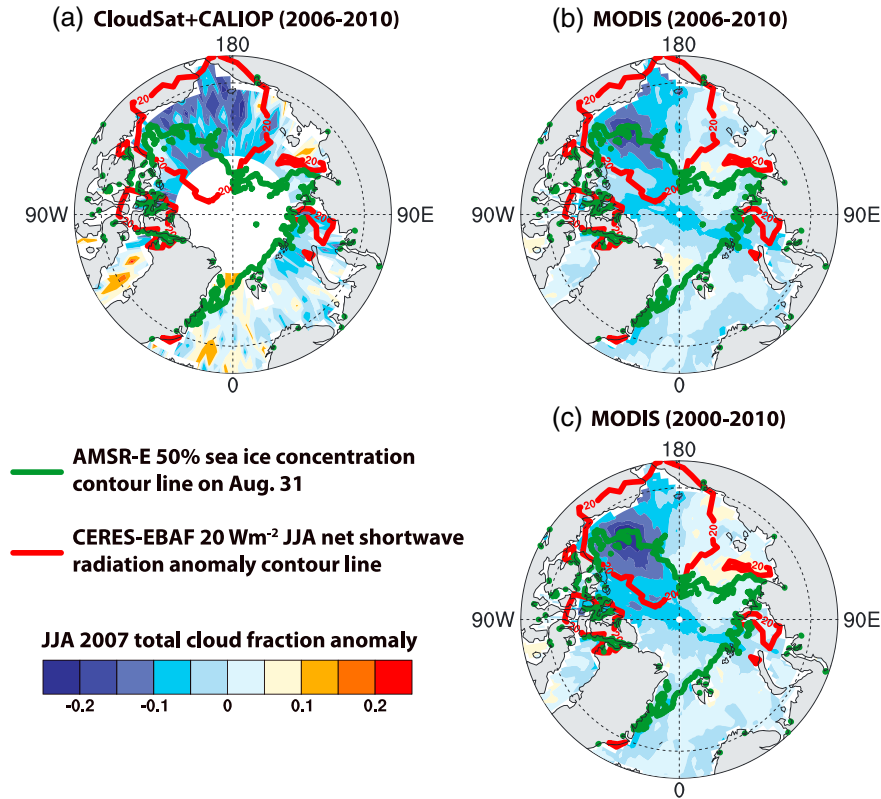


Figure 11. Summer (JJA) 2007 total cloud fraction anomalies: (a) CloudSat + CALIPSO 2007 anomaly from 2006 to 2010, (b) MODIS 2007 anomaly from 2006 to 2010, and (c) MODIS 2007 anomaly from 2000 to 2010. The figure uses CERES-EBAF data available from March 2000 to February 2011 (Table 1), CloudSat and CALIPSO data available from July 2006 to February 2011 (Table 1), and daily sea ice extents from AMSR-E observations [Cavalieri *et al.*, 2004].

of fluxes are limited. We begin by validating 2B-FLXHR-LIDAR shortwave flux calculations using CERES-EBAF observations. Comparison of CERES-EBAF observed anomalies and 2B-FLXHR-LIDAR calculated anomalies over the same time period (July 2006 to February 2011) and Arctic Ocean domain (70° – 82° N) shows the mean summer 2007 TOA net shortwave radiation anomalies are 2 W m^{-2} larger in CERES-EBAF observations ($+10 \text{ W m}^{-2}$) than in 2B-FLXHR-LIDAR calculations ($+8 \text{ W m}^{-2}$). Nevertheless, visual comparison reveals impressive agreement between the spatial patterns of observed and calculated anomalies (Figure 12). Unlike for the cloud anomalies shown in Figure 11, the base time period used for radiation anomalies was important to consider, an unsurprising factor given the decreasing TOA albedo trend shown in Figure 8a. Indeed, when the full CERES-EBAF time period (2000–2010) is used for anomaly calculations, the summer 2007 net shortwave radiation anomalies are substantially larger than those when the 2006–2010 time period is used ($+12 \text{ W m}^{-2}$ versus $+7 \text{ W m}^{-2}$ for the Arctic Ocean average). The 2B-FLXHR calculations indicate that atmospheric absorption anomalies during summer 2007 were small. As a result, 2B-FLXHR-LIDAR net shortwave flux anomalies have similar magnitude at the TOA and at the surface. This result suggests that TOA evaluation of 2B-FLXHR-LIDAR calculations with CERES-EBAF observations also has relevance for surface 2B-FLXHR-LIDAR calculations.

[39] A useful asset of the 2B-FLXHR-LIDAR algorithm framework is the ability to do off-line sensitivity studies. To take advantage of this asset, we used the 2B-FLXHR-LIDAR algorithm to generate a second set of flux estimates driven by a fixed climatological mean annual cycle of surface albedo. Through comparison of these fixed-albedo flux calculations with the standard 2B-FLXHR-LIDAR time-varying albedo flux calculations, the relative contributions of atmospheric and surface anomalies to radiation anomalies can be assessed. We applied this methodology to summer 2007. For reference, the average summer surface albedos used for the fixed-albedo and standard time-varying albedo 2B-FLXHR-LIDAR flux calculations are compared in Figure 13. Over the central Arctic, the surface albedo values during 2007 used in the standard time-varying albedo flux calculations (Figure 13a) are much lower than the climatological values used in the fixed-albedo flux calculations (Figure 13b). A comparison of the corresponding radiative fluxes is shown in Figure 14. In agreement with the monthly mean spatial relationships in Figure 10, the off-line sensitivity test indicates that both atmospheric and surface anomalies contributed to summer 2007 shortwave radiation anomalies.

[40] To begin, we describe the summer 2007 surface radiation anomalies in the 2B-FLXHR-LIDAR calculations with variable surface albedo. Over much of the Arctic Ocean, Figures 14a and 14b show that positive net surface

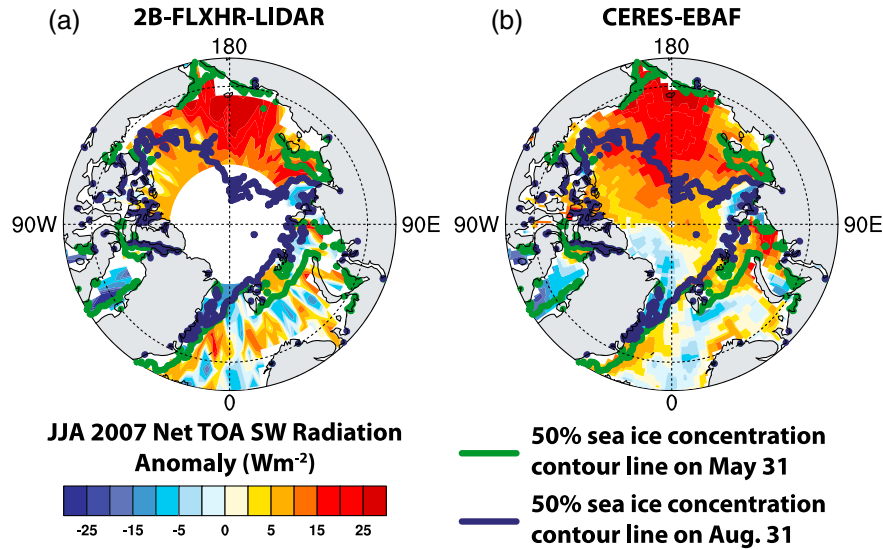


Figure 12. Polar maps of summer (JJA) 2007 net TOA shortwave radiation anomalies: (a) 2B-FLXHR-LIDAR and (b) CERES-EBAF. The figure uses 2B-FLXHR and CERES-EBAF data available from July 2006 to February 2011 (Table 1).

shortwave radiation anomalies of up to $+40 \text{ W m}^{-2}$ are significantly larger than more variable net surface longwave radiation anomalies.

[41] We next present radiative fluxes from 2B-FLXHR-LIDAR calculations with a fixed climatological albedo in Figures 14c and 14d. Because the calculations used to generate Figures 14c and 14d utilize 2007 atmospheric conditions but climatological surface conditions, they isolate the influence of summer 2007 atmospheric anomalies on summer 2007 radiative flux anomalies. North of Alaska and the Bering Strait, Figure 14c shows that shortwave radiation anomalies resulting from the 2007 atmospheric anomalies alone often exceeded $+10 \text{ W m}^{-2}$. Comparison with Figure 11 suggests that cloud reductions are responsible for these positive shortwave radiation anomalies. North of Siberia and along the dateline (180°E), Figure 14d shows surface net longwave radiation was anomalously large, a result that is inconsistent with

weak or negative cloud anomalies in Figure 11. Thus, the influence of the 2007 atmosphere on anomalously large net longwave radiation may instead be explained by noncloud atmospheric variables. Noncloud candidates that could explain the increased net surface longwave radiation during summer 2007 include anomalously high temperatures and water vapor amounts associated with anomalous warm air advection [e.g., Kay *et al.*, 2008; Graverson *et al.*, 2010].

[42] To complete presentation of the 2B-FLXHR-LIDAR off-line sensitivity test, Figures 14e and 14f show the difference between the 2B-FLXHR-LIDAR calculations with fixed and variable surface albedos. Because differencing removes the influence of the 2007 atmospheric anomalies on radiative flux anomalies, Figures 14e and 14f isolate the influence of the 2007 surface anomalies on summer 2007 radiative flux anomalies. North of Siberia and the Bering Strait (115°E to 160°W), anomalously low sea ice cover in 2007

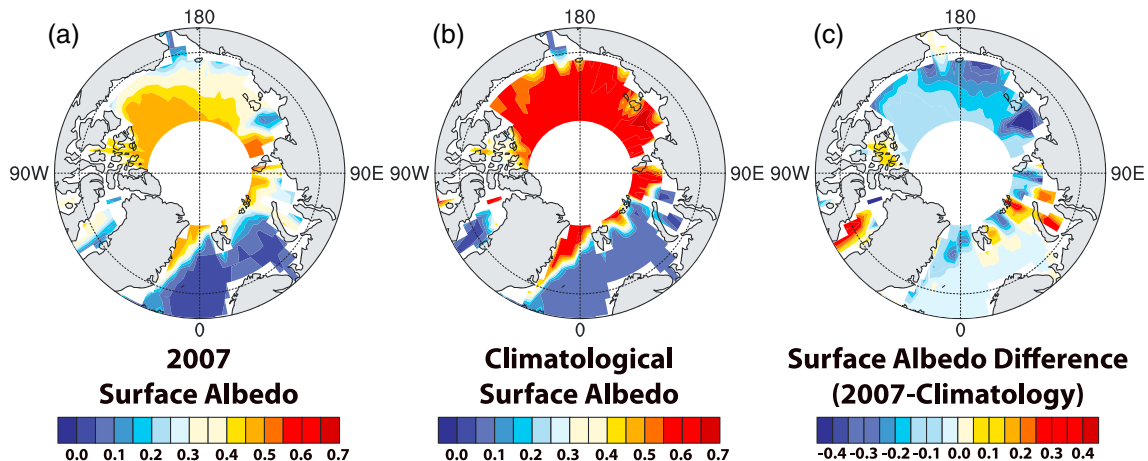


Figure 13. Polar maps of summer (JJA) surface albedo used in 2B-FLXHR-LIDAR calculations shown in Figure 14: (a) 2007, (b) climatology, and (c) difference between 2007 and climatology.

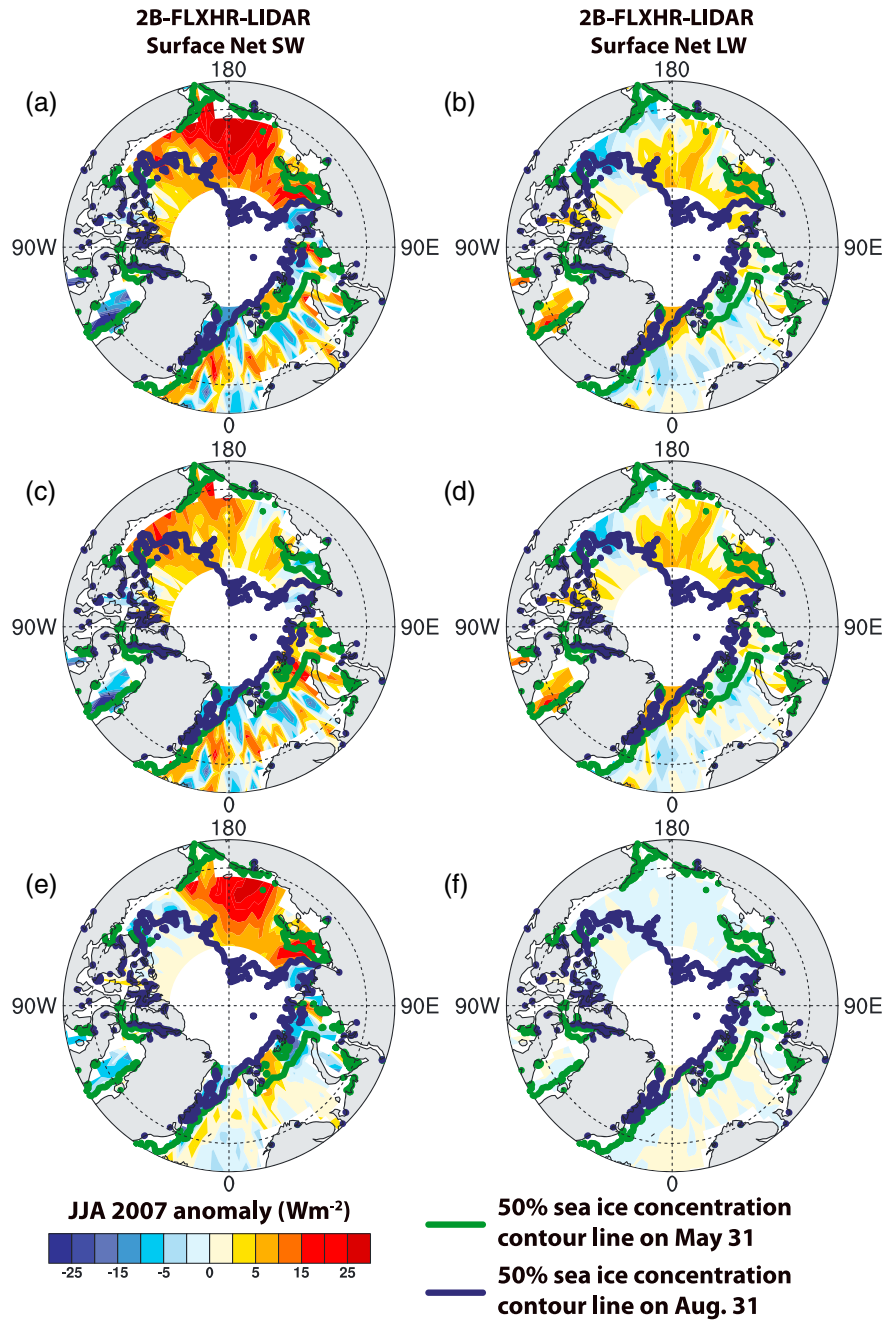


Figure 14. Polar maps of 2B-FLXHR-LIDAR summer (JJA) 2007 anomalies. (a) Net shortwave surface radiation, (b) net longwave surface radiation, (c) influence of 2007 atmosphere on net shortwave surface radiation (fixed climatological albedo), (d) influence of 2007 atmosphere on net longwave surface radiation (fixed climatological albedo), (e) influence of 2007 surface on net shortwave surface radiation, and (f) influence of 2007 surface on net longwave surface radiation. The figure uses 2B-FLXHR-LIDAR data available from July 2006 to February 2011 (Table 1) and daily sea ice extents from AMSR-E observations [Cavalieri *et al.*, 2004]. Figures 14a, 14b, 14e, and 14f use the 2007 surface albedos in Figure 13a. Figures 14c and 14d use the climatological surface albedos in Figure 13b.

resulted in positive net shortwave radiation anomalies to as high as $+35 \text{ W m}^{-2}$. In these same regions, downwelling shortwave radiation was anomalously low due to reduced multiple scattering between the relatively dark surface and overlying clouds (not shown). As expected, Figure 14f shows the influence of the surface on summer 2007 longwave radiation anomalies was negligible.

4. Discussion

[43] The early 21st century climatology presented in this study provides new observational constraints on domain-wide Arctic Ocean clouds and radiative fluxes during a period of accelerated Arctic change. The annual mean cloud forcing results are qualitatively consistent with previous

findings that Arctic clouds warm the surface and cool the TOA [e.g., *Intieri et al.*, 2002; *Dong et al.*, 2010; *Schweiger and Key*, 1994; *Zygmuntowska et al.*, 2012]; however, the quantitative values differ from previous studies. Unfortunately, direct comparison between cloud forcing estimates in multiple studies is challenging due to differences in temporal and geographic sampling.

[44] Prior to CloudSat+CALIPSO-based products, the only estimates of Arctic surface cloud forcing that relied on combined radar and lidar remote sensing observations were from a single year of ship-based observations on an Arctic Ocean drifting platform located primarily in the Beaufort Sea (Surface Heat Budget of the Arctic Ocean (SHEBA) during 1997) [*Intieri et al.*, 2002] and from 10 years of land-based observations at Barrow, Alaska (Atmospheric Radiation Measurement North Slope of Alaska (ARM NSA) [*Dong et al.*, 2010]). Annual mean Arctic Ocean surface cloud warming in 2B-FLXHR-LIDAR ($+10 \text{ W m}^{-2}$) is smaller than the SHEBA estimates ($+28 \text{ W m}^{-2}$) [*Intieri et al.*, 2002] but larger than the ARM NSA estimates ($+3.5 \text{ W m}^{-2}$) [*Dong et al.*, 2010]. The influence of land on cloud cover and on surface albedo makes comparison between the ARM NSA estimates and Arctic Ocean estimates difficult to interpret. Geographic and temporal variations in cloud forcing contribute to differences between the 2B-FLXHR-LIDAR Arctic Ocean average and the SHEBA cloud forcing estimates. The marginal seas on the Pacific side of the Arctic, including the SHEBA region ($70\text{--}80^\circ\text{N}$, 130 to 170°W), have more positive surface cloud forcing than the average over the Arctic Ocean domain (Figure 4). If we average 2B-FLXHR-LIDAR over the SHEBA region, the 2B-FLXHR-LIDAR cloud forcing estimates ($+12 \text{ W m}^{-2}$ total, -22 W m^{-2} shortwave, and $+34 \text{ W m}^{-2}$ longwave) are slightly closer to the SHEBA cloud forcing estimates ($+28 \text{ W m}^{-2}$ total, -10 W m^{-2} shortwave, and $+38 \text{ W m}^{-2}$ longwave) but are still quite different, especially in the shortwave. The stronger shortwave cloud cooling over the SHEBA region in the 2B-FLXHR-LIDAR data set is consistent with lower surface albedos due to less sea ice cover during 2006–2010 than during the year of the SHEBA experiment (1997).

[45] Differences between 2B-FLXHR-LIDAR and previous basin-wide estimates of Arctic cloud forcing are also important to understand. Although a direct comparison of overlapping time periods is not possible, it is interesting that annual mean TOA forcing in 2B-FLXHR-LIDAR lies within 2 W m^{-2} of Arctic-wide estimates based on the International Satellite Cloud Climatology Project (ISCCP) C2 data set (-10 W m^{-2}) [*Schweiger and Key*, 1994]. In contrast, the annual mean surface forcing in 2B-FLXHR-LIDAR is 16 W m^{-2} smaller at the surface than the ISCCP-based estimate ($+26 \text{ W m}^{-2}$) [*Schweiger and Key*, 1994]. When compared over the same domain ($68\text{--}82^\circ\text{N}$, $100\text{--}330^\circ\text{E}$), monthly 2B-FLXHR-LIDAR Arctic Ocean cloud forcing is stronger than the mean of the range of an estimate using CloudSat clouds alone [*Zygmuntowska et al.*, 2012, Figure 5]. During late summer and fall, the 2B-FLXHR-LIDAR cloud forcing presented here exceeds the uncertainty range provided in *Zygmuntowska et al.* [2012] by up to 20 W m^{-2} . These differences underscore the importance of reliable and comprehensive cloud detection for cloud radiative forcing calculations and the new contribution of the 2B-FLXHR-LIDAR calculations presented here.

[46] We found complex relationships between clouds, sea ice, and shortwave radiation during the early 21st century. The relatively long time series provided by MODIS and CERES-EBAF was essential for assessing cloud influence on shortwave radiation trends and variability. Similar to an analysis of 2000–2004 trends in *Kato et al.* [2006], our analysis of 2000–2010 trends showed that reduced summer sea ice extent is leading to increased summer net TOA shortwave radiation. Unlike in the *Kato et al.* [2006] trend analysis, our summer trend analysis using identical data sets but with 6 additional years of observations provides no evidence of summer cloud trends influencing summer shortwave radiation trends during the early 21st century. In other words, as in *Kay and Gettelman* [2009], we found no summer cloud response to or feedback on summer Arctic sea ice loss. Because the cloud response to sea ice loss varies with season [*Kay and Gettelman*, 2009], assessing the cloud response to sea ice loss should be done using seasonal or subseasonal averages. For example, *Liu et al.* [2012] average from July to November and report a cloudier Arctic with diminishing sea ice. While not necessarily at odds with the results here, the *Liu et al.* [2012] results are confusing because they mix together summer when we find no evidence for a cloud response to sea ice loss and fall when cloud amounts are increasing over regions with sea ice loss [*Kay and Gettelman*, 2009; *Wu and Lee*, 2012].

[47] While we found no evidence for summer cloud trends, summer cloud variability was important for summer shortwave radiative flux variability. Similar to the results reported in *Qu and Hall* [2005], both atmosphere (clouds) and surface contributions contribute to variability in TOA albedo over the Arctic Ocean. The results here also hint that during the early 21st century, clouds were more important for explaining early summer TOA albedo variability, while sea ice loss was more important for explaining late summer TOA albedo variability.

[48] The most important observational constraint presented in this climatology is TOA radiative fluxes from CERES-EBAF. To our knowledge, the use of these Arctic Ocean radiation observations to evaluate the mechanisms underlying the 2007 summer Arctic sea ice anomalies is new. The CERES-EBAF observations reveal large net shortwave radiation anomalies during all 3 months of summer 2007, especially during June and July.

[49] Because CERES-EBAF observations are the only radiation observations available over the entire Arctic Basin, the summer 2007 anomalies shown in Figures 10a–10c and 12b are a unique benchmark for evaluating Arctic Ocean radiative transfer calculations. We have used CERES-EBAF observations to evaluate our observationally constrained radiative transfer calculations (Figures 6 and 12) and have found agreement within the combined uncertainty estimates. Previous studies evaluating the contribution of cloud and shortwave radiation anomalies to sea ice loss have not used CERES-EBAF for validation and thus have relied on radiative flux calculations of unknown quality over the Arctic Ocean [*Kay et al.*, 2008; *Nussbaumer and Pinker*, 2012; *Schweiger et al.*, 2008; *Graversen et al.*, 2010].

[50] Do the observations presented here change our understanding of the mechanisms leading to record sea ice loss during summer 2007? The broad consensus is that multiple factors lead to the 2007 sea ice minimum [*Kay et al.*, 2008; *Zhang et al.*, 2008; *Lindsay et al.*, 2009; *Kauker et al.*,

2009; Stroeve *et al.*, 2011; Ogi and Wallace, 2012]. Thus, the open question is as follows: Did cloud and shortwave radiation anomalies contribute to summer 2007 sea ice loss? The literature has been divided with some studies suggesting that shortwave radiation and cloud anomalies contributed to sea ice loss [Kay *et al.*, 2008; Perovich *et al.*, 2008] and others suggesting that shortwave radiation and cloud anomalies played no role [Schweiger *et al.*, 2008] or were even of the opposite sign [Graverson *et al.*, 2010]. The new observations analyzed in this study enable a critical evaluation of the methods and data sets underlying these previous studies.

[51] While the impacts of cloud and radiation anomalies on sea ice are not quantified in this study, the observational constraints documented in this study are consistent with the hypothesis that clouds and shortwave radiation anomalies contributed to the 2007 sea ice loss. Most importantly, the observations of radiative fluxes shown here challenge the observational basis of previous studies that found cloud and associated shortwave radiation anomalies were unimportant. For example, Schweiger *et al.* [2008] used cloud fraction anomalies that are much smaller than those in Figure 11. Most importantly, the 2007 shortwave radiation anomalies used by Schweiger *et al.* [2008] are based on a simple parameterization that relates cloud fraction to shortwave radiation, and should be evaluated with the observations in Figure 10. Similarly, Graverson *et al.* [2010] analyzed reanalysis (ERA-Interim) radiative transfer calculations, which have smaller shortwave radiative flux anomalies with different patterns than the observations shown in Figure 10.

[52] While the synergy of multiple data sets has advanced our observational constraints on Arctic Ocean clouds and radiative fluxes in the last decade, observational gaps limit our understanding on the timescales that are relevant. For example, the most reliable cloud data set (CloudSat + CALIPSO) has inadequate sampling to provide a subseasonal perspective, but it was only by using monthly observations that we were able to isolate the influence of atmospheric (cloud) and surface conditions on radiation anomalies (Figure 10). While sensitivity tests within the 2B-FLXHR-LIDAR framework were able to separate the atmospheric and surface contributions to surface radiation anomalies, they are still quite noisy due to poor sampling (Figure 14). Finally, unlike atmospheric forcing over land, atmospheric forcing over the ocean requires a Lagrangian perspective because sea ice moves with the ocean currents. In other words, a static seasonal view can be misleading if your goal is to evaluate the influence of atmospheric forcing on sea ice. For example, given the wind patterns of summer 2007, sea ice that experienced the shortwave radiation anomalies in June and July 2007 above Alaska was advected by the strong anomalous Beaufort High. Yet, this perspective was missing from previous studies that assumed a direct spatial correlation between atmospheric forcing and ice loss on seasonal timescales [e.g., Kay *et al.*, 2008; Graverson *et al.*, 2010; Nussbaumer and Pinker, 2012]. Because the sea ice Lagrangian perspective is important, Arctic Ocean observations with high temporal and geographic resolution perspective are especially needed.

5. Summary

[53] This study uses unique multisensor Arctic Ocean observations to create a cloud and radiation climatology for

the early 21st century (March 2000 to February 2011). The analyzed data sets include the following: (1) a spaceborne radar and lidar cloud data set (CloudSat + CALIPSO), (2) a cloud data set with known limitations in Arctic regions but monthly temporal frequency (MODIS), (3) observed radiative fluxes (CERES-EBAF), (4) observationally constrained radiative flux calculations (FLXHR-LIDAR), and (5) two independent observationally constrained cloud forcing estimates (2B-FLXHR-LIDAR and CERES-EBAF).

[54] Several robust findings emerge from analysis of this Arctic Ocean climatology.

[55] 1. On annual average, 2B-FLXHR-LIDAR calculations show Arctic Ocean clouds warm the surface (10 W m^{-2} total, -32 W m^{-2} shortwave, and 42 W m^{-2} longwave) and cool the top of atmosphere (-12 W m^{-2} total, -31 W m^{-2} shortwave, and 19 W m^{-2} longwave). Despite their identical annual mean total TOA cloud forcing estimates (-12 W m^{-2}), 2B-FLXHR-LIDAR has both stronger shortwave cloud forcing and longwave cloud forcing than CERES-EBAF, differences that appear in part related to the improved cloud detection and increased cloud amounts in 2B-FLXHR-LIDAR.

[56] 2. Arctic Ocean clouds have differing influences on summer shortwave radiation trends and variability. During the early 21st century, increasing net summer shortwave radiation and decreasing TOA albedo trends are consistent with sea ice loss but are unrelated to summer cloud amounts. In contrast, summer cloud and summer sea ice variability both contribute to summer shortwave radiation variability.

[57] 3. The remarkable nature of summer 2007 Arctic Ocean anomalies is evident in this study. During that summer, observations from CERES-EBAF show positive TOA shortwave radiation anomalies exceeded 20 W m^{-2} over much of the Arctic Ocean. Both cloud reductions and sea ice loss are required to explain the observed anomalous shortwave radiation absorption with cloud reductions being the dominant contributor during early summer and sea ice loss being the dominant contributor during late summer.

[58] 4. There is a continued need for sustained and also improved measurement of Arctic clouds, surface albedo, and radiative fluxes. Cloud properties (water content, particle size, and thickness) and, to a lesser extent, surface albedo emerge as the key uncertainties in the observationally constrained Arctic Ocean radiative flux calculations analyzed here and one that future studies could improve upon. High-quality and high temporal frequency (at least monthly) Arctic-wide observations are essential for enhancing understanding the relationships between clouds, sea ice, and radiation.

[59] **Acknowledgments.** The authors thank Chris O'Dell for processing and providing MODIS observations and Andrew Gettelman, Jason English, and Ed Blanchard-Wrigglesworth for fruitful discussions. This research was supported by NASA grant 09-CCST09-29.

References

- Barton, N. P., S. A. Klein, J. S. Boyle, and Y. Y. Zhang (2012), Arctic synoptic regimes: Comparing domain-wide Arctic cloud observations with CAM4 and CAM5 during similar dynamics, *J. Geophys. Res.*, **117**, D15205, doi:10.1029/2012JD017589.
- Beesley, J. A., and R. E. Moritz (1999), Toward an explanation of the annual cycle of cloudiness over the Arctic Ocean, *J. Clim.*, **12**, 395–415.
- Bowker, D. E., R. E. Davis, D. L. Myrick, K. Stacy, and W. T. Jones (1985), Spectral reflectances of natural targets for use in remote sensing studies, NASA Ref. Publ., 1139.
- Briegleb, B. P., and V. Ramanathan (1982), Spectral and diurnal variations in clear sky planetary albedo, *J. Appl. Meteorol.*, **21**, 1160–1171.

- Cavaleri, D., T. Markus, and J. Comiso (2004), AMSR-E/Aqua daily L3 12.5 km brightness temperature, sea ice concentration, and snow depth polar grids V002, June–August 2007, http://nsidc.org/data/docs/daac/ae_si12_12km_tb_sea_ice_and_snow.gd.html, Natl. Snow and Ice Data Cent., Boulder, Colo. [Updated daily].
- Cesana, G., J. E. Kay, H. Chepfer, J. M. English, and G. de Boer (2012), Ubiquitous low-level liquid-containing Arctic clouds: New observations and climate model constraints from CALIPSO-GOCCP, *Geophys. Res. Lett.*, **39**, L20804, doi:10.1029/2012GL053385.
- Dong, X., B. Xi, K. Crosby, C. N. Long, R. S. Stone, and M. D. Shupe (2010), A 10 year climatology of Arctic cloud fraction and radiative forcing at Barrow, Alaska, *J. Geophys. Res.*, **115**, D17212, doi:10.1029/2009JD013489.
- Eastman, R., and S. G. Warren (2010), Interannual variations of Arctic cloud types in relation to sea ice, *J. Clim.*, **23**, 4216–4232, <http://dx.doi.org/10.1175/2010JCLI3492.1>.
- Fetterer, F., K. Knowles, W. Meier, and M. Savoie (2002), Sea ice index, http://nsidc.org/data/docs/noaa/g02135_seaice_index/, Natl. Snow and Ice Data Cent., Boulder, Colo. [Updated 2009].
- Gottelman, A., V. P. Walden, L. M. Miloshevich, W. L. Roth, and B. Halter (2006), Relative humidity over Antarctica from radiosondes, satellites and a general circulation model, *J. Geophys. Res.*, **111**, D09S13, doi:10.1029/2005JD006636.
- Graversen, R. G., T. Mauritsen, S. Drijfhout, M. Tjernström, and S. Mårtensson (2010), Warm winds from the Pacific caused extensive Arctic sea-ice melt in summer 2007, *Clim. Dyn.*, **36**, 2103–2112, doi:10.1007/S00382-010-0809-Z.
- Henderson, D. S., T. L'Ecuyer, G. Stephens, P. Partain, and M. Sekiguchi (2013), A multi-sensor perspective on the radiative impacts of clouds and aerosols, *J. Appl. Meteorol. Climatol.*, **52**, 853–871, doi:10.1175/JAMC-D-12-025.1.
- Hudson, S. R. (2011), Estimating the global radiative impact of the sea ice-albedo feedback in the Arctic, *J. Geophys. Res.*, **116**, D16102, doi:10.1029/2011JD015804.
- Intieri, J. M., C. W. Fairall, M. D. Shupe, P. O. G. Persson, E. L. Andreas, P. S. Guest, and R. E. Moritz (2002), An annual cycle of Arctic surface cloud forcing at SHEBA, *J. Geophys. Res.*, **107**(C10), 8039, doi:10.1029/2000JC000439.
- Kato, S., N. G. Loeb, P. Minnis, J. A. Francis, T. P. Charlock, D. A. Rutan, E. E. Clothiaux, and S. Sun-Mack (2006), Seasonal and interannual variations of top-of-atmosphere irradiance and cloud cover over polar regions derived from the CERES data set, *Geophys. Res. Lett.*, **33**, L19804, doi:10.1029/2006GL026685.
- Kauker, F., T. Kaminski, M. Karcher, R. Giering, R. Gerdes, and M. Voßbeck (2009), Adjoint analysis of the 2007 all time Arctic sea-ice minimum, *Geophys. Res. Lett.*, **36**, L03707, doi:10.1029/2008GL036323.
- Kay, J. E., and A. Gettelman (2009), Cloud influence on and response to seasonal Arctic sea ice loss, *J. Geophys. Res.*, **114**, D18204, doi:10.1029/2009JD011773.
- Kay, J. E., T. L'Ecuyer, A. Gettelman, G. Stephens, and C. O'Dell (2008), The contribution of cloud and radiation anomalies to the 2007 Arctic sea ice extent minimum, *Geophys. Res. Lett.*, **35**, L08503, doi:10.1029/2008GL033451.
- Kay, J. E., M. M. Holland, and A. Jahn (2011), Inter-annual to multi-decadal Arctic sea ice extent trends in a warming world, *Geophys. Res. Lett.*, **38**, L15708, doi:10.1029/2011GL048008.
- L'Ecuyer, T. S., and J. Jiang (2010), Touring the atmosphere aboard the A-train, *Phys. Today*, **63**, 36–41.
- L'Ecuyer, T. S., N. Wood, T. Haladay, and G. L. Stephens (2008), The impact of clouds on atmospheric heating based on the R04 CloudSat fluxes and heating rate dataset, *J. Geophys. Res.*, **113**, D00A15, doi:10.1029/2008JD009951.
- Lindsay, R. W., J. Zhang, A. Schweiger, M. A. Steele, and H. Stern (2009), Arctic sea ice retreat in 2007 follows thinning trend, *J. Clim.*, **22**, 165–176, doi:10.1175/2008JCLI2521.
- Liu, Y. H., S. A. Ackerman, B. C. Maddux, J. R. Key, R. A. Frey (2010), Errors in cloud detection over the Arctic using a satellite imager and implications for observing feedback mechanisms, *J. Clim.*, **23**(7), 1894–1907.
- Liu, Y., J. R. Key, Z. Liu, and X. Wang, and S. J. Vavrus (2012), A cloudier Arctic expected with diminishing sea ice, *Geophys. Res. Lett.*, **39**, L05705, doi:10.1029/2012GL051251.
- Loeb, N. G., B. A. Wielicki, D. R. Doelling, G. L. Smith, D. F. Keyes, S. Kato, N. Manalo-Smith, and T. Wong (2009), Toward optimal closure of the Earth's top-of-atmosphere radiation budget, *J. Clim.*, **22**, 748–766, doi:10.1175/2008JCLI2637.1.
- Mace, G. G., Q. Zhang, M. Vaughan, R. Marchand, G. Stephens, C. Trepte, and D. Winker (2009), A description of hydrometeor layer occurrence statistics derived from the first year of merged CloudSat and CALIPSO data, *J. Geophys. Res.*, **114**, D00A26, doi:10.1029/2007JD009755.
- Marchand, R., G. G. Mace, T. Ackerman, and G. Stephens (2008), Hydrometeor detection using CloudSat—An Earth-orbiting 94-GHz cloud radar, *J. Appl. Meteorol. Climatol.*, **25**(4), 519–533.
- Nolin, A., R. L. Armstrong, and J. Maslanik (1998), *Near-Real-Time SSM/I-SSMIS EASE-Grid Daily Global Ice Concentration and Snow Extent*, Version 4, http://nsidc.org/data/docs/daac/nise1_nise.gd.html, Natl. Snow and Ice Data Cent., Boulder, Colorado USA [Updated daily].
- Nussbaumer, E. A., and R. T. Pinker (2012), The role of shortwave radiation in the 2007 Arctic sea ice anomaly, *Geophys. Res. Lett.*, **39**, L15808, doi:10.1029/2012GL052415.
- Ogi, M., and J. M. Wallace (2012), The role of summer surface wind anomalies in the summer Arctic sea ice extent in 2010 and 2011, *Geophys. Res. Lett.*, **39**, L09704, doi:10.1029/2012GL051330.
- Palm, S. P., S. T. Strey, J. Spinhirne, and T. Markus (2010), Influence of Arctic sea ice extent on polar cloud fraction and vertical structure and implications for regional climate, *J. Geophys. Res.*, **115**, D21209, doi:10.1029/2010JD013900.
- Perovich, D. K., and C. Polashenski (2012), Albedo evolution of seasonal Arctic sea ice, *Geophys. Res. Lett.*, **39**, L08501, doi:10.1029/2012GL051432.
- Perovich, D. K., J. A. Richter-Menge, K. F. Jones, and B. Light (2008), Sunlight, water, and ice: Extreme Arctic sea ice melt during the summer of 2007, *Geophys. Res. Lett.*, **35**, L11501, doi:10.1029/2008GL034007.
- Platnick, S., M. D. King, S. A. Ackerman, W. P. Menzel, B. A. Baum, J. C. Riedi, and R. A. Frey (2003), The MODIS cloud products: Algorithms and examples from Terra, *IEEE Trans. Geosci. Remote Sens.*, **41**(2), 459–473.
- Qu, X., and A. Hall (2005), Surface contribution to planetary albedo variability in cryosphere regions, *J. Clim.*, **18**, 5239–5252, <http://dx.doi.org/10.1175/JCLI3555.1>.
- Ramanathan, V., R. D. Cess, E. F. Harrison, P. Minnis, B. R. Barkstrom, E. Ahmad, and D. Hartmann (1989), Radiative forcing and climate: Results from the Earth Radiation Budget Experiment, *Science*, **243**(4887), 57–63, doi:10.1126/science.243.4887.57.
- Schweiger, A. J., and J. R. Key (1994), Arctic Ocean radiative fluxes and cloud forcing estimated from the ISCCP C2 cloud dataset, 1983–1990, *J. Appl. Meteorol.*, **33**, 948–963.
- Schweiger, A. J., J. Zhang, R. W. Lindsay, and M. Steele (2008), Did unusually sunny skies help drive the record sea ice minimum of 2007?, *Geophys. Res. Lett.*, **35**, L10503, doi:10.1029/2008GL033463.
- Serreze, M. C., M. M. Holland, and J. Stroeve (2007), Perspectives on the Arctic's shrinking sea-ice cover, *Science*, **315**(5818), 1533–1536, doi:10.1126/science.1139426.
- Stephens, G. L., et al. (2008), CloudSat mission: Performance and early science after the first year of operation, *J. Geophys. Res.*, **113**, D00A18, doi:10.1029/2008JD009982.
- Stroeve, J. C., M. C. Serreze, M. M. Holland, J. E. Kay, W. Meier, and A. P. Barrett (2011), The Arctic's rapidly shrinking sea ice cover: A research synthesis, *Clim. Change*, **110**(3–4), 1005–1027, doi:10.1007/s10584-011-0101-1.
- Wu, D. L., and J. N. Lee (2012), Arctic low cloud changes as observed by MISR and CALIOP: Implication for the enhanced autumnal warming and sea ice loss, *J. Geophys. Res.*, **117**, D07107, doi:10.1029/2011JD017050.
- Zhang, J., R. Lindsay, M. Steele, and A. Schweiger (2008), What drove the dramatic retreat of Arctic sea ice during summer 2007? *Geophys. Res. Lett.*, **35**, L11505, doi:10.1029/2008GL034005.
- Zygmuntowska, M., T. Mauritsen, J. Quaas, and L. Kaleschke (2012), Arctic clouds and surface radiation—A critical comparison of satellite retrievals and the ERA-Interim reanalysis, *Atmos. Chem. Phys.*, **12**, 6667–6677, doi:10.5194/ACP-12-6667-2012.